Mon. Not. R. Astron. Soc. **000**, 1–20 (2002) Printed 17 December 2013 (MN LATEX style file v2.2)

General relativistic modelling of the negative reverberation X-ray time delays in AGN⋆

D. Emmanoulopoulos,[1]† I. E. Papadakis,[2,3] M. Dovčiak[4] and I. M. McHardy[1]
[1] *Physics and Astronomy, University of Southampton, Southampton, SO17 1BJ, UK*
[2] *Department of Physics and Institute of Theoretical and Computational Physics, University of Crete, 71003 Heraklion, Greece*
[3] *IESL, Foundation for Research and Technology, 71110 Heraklion, Greece*
[4] *Astronomical Institute of the Academy of Sciences, Boční II 1401, CZ-14100 Praha 4, Czech Republic*

Accepted 2013 Month 31. Received – 2013 December 17; in original form – 2013 December 17

ABSTRACT
We present the first systematic physical modelling of the time-lag spectra between the soft (0.3–1 keV) and the hard (1.5–4 keV) X-ray energy bands, as a function of Fourier frequency, in a sample of 12 AGN which have been observed by *XMM-Newton*. We concentrate particularly on the negative X-ray time-lags (NXTLs), i.e. soft band variations lag the hard band variations, which are seen at high Fourier frequencies. We assume a lamp-post X-ray source geometry and that soft X-rays are produced by reprocessing and reflection by the accretion disc. We also assume that the response of the accretion disc, in the soft X-ray bands, is adequately described by the response in the neutral Fe Kα line at 6.4 keV. We use fully general relativistic ray-tracing simulations to determine impulse response functions for the Fe Kα line. Then, from these functions we derive corresponding time-lag spectral models which we fit to the observations. The general relativistic impulse response functions (GRIRFs), and thus the corresponding time-lag spectra, depend on the black hole (BH) mass, M, BH spin parameter, α, viewing angle, θ, and height, h, of the X-ray source above the disc. Additionally we parametrize the time-lag spectra at low Fourier frequencies (typically lower than 10^{-4} Hz), where the time delays are positive, by a power-law. These, physically based GRIRFs, yield much more realistic results than the commonly-used, but erroneous, top-hat parametric models. We find that the best-fitting BH masses agree quiet well with those derived by other methods, thus providing us with a new tool for BH mass determination. We also find that, for all of our AGN sample, the X-ray sources lie only around 3.7 gravitational radii above the accretion discs. We find no evidence for any correlation between M and either α, θ or h. Moreover, there is a tentative indication that the BH spin distribution may be bimodal, with a high spin and a low spin group above and below 0.62. Finally, the viewing angles are distributed uniformly between 20 and 60°.

Key words: galaxies: active – galaxies: nuclei – X-rays: galaxies – accretion,accretion disks – black hole physics – relativistic processes

1 INTRODUCTION

In the current paradigm, active galactic nuclei (AGN) contains a central black hole (BH) which is fed, in most cases, by an optically thick and geometrically thin accretion disc as a result of matter transportation inwards and angular momentum outwards. This disc radiates as a series of black-body components (Shakura & Sunyaev 1973) with peak emission at optical-ultraviolet wavelengths (Malkan 1983). Part of this radiation is assumed to be Compton up-scattered within a mildly relativistic hot electron cloud often called the *X-ray corona*. This medium is assumed to be located above the disc. It is often approximated as a point source (representing the centroid of the X-ray emitting source), lying above the central BH, on the axis of symmetry of the system (i.e. BH spin axis). This arrangement is known as the '*lamp-post geometry*'.

The photons, from the X-ray source, form a power-law spectrum. Depending on the location of the X-ray source, a

⋆ Based on observations obtained with *XMM-Newton*, an ESA science mission with instruments and contributions directly funded by ESA Member States and NASA.
† E-mail: D.Emmanoulopoulos@soton.ac.uk

substantial part of the primary X-ray flux may illuminate the accretion disc. In this case, they are either Compton scatted by free or bound electrons, or photoelectrically absorbed followed by fluorescent line emission, or by Auger de-excitation. This yields the so-called 'reflection spectrum' consisting of a number of emission and absorption lines (mainly below 1 keV), together with the 6.4 keV Fe Kα emission line from neutral material, which is the strongest feature (George & Fabian 1991).

Depending on the proximity of the reflection process to the BH, the various lines can undergo relativistic broadening (Fabian et al. 1989; Laor 1991). These relativistically broadened lines may account for the observed *soft X-ray excess* (Crummy et al. 2006), where the X-ray data below 1 keV (soft band) lie above the power-law extrapolation of the continuum, usually measured in the 1.5–4 keV (hard band). However, alternative interpretations for the soft excess are also possible e.g. Comptonisation of disc photons from the X-ray source (Page et al. 2004), Comptonisation of disc photons within a hot layer on the accretion disc (Wang & Netzer 2003; Done et al. 2012).

In addition to the primary and the reflected component, several AGN exhibit absorption features in their X-ray spectra as well. These feature can arise by: i) outflows which are either thermally or radiatively or magnetically driven winds (Cappi 2006) and can reach mildly relativistic speeds (Tombesi et al. 2010), ii) inflows (Krug et al. 2010), and iii) X-ray absorption clouds (Risaliti et al. 2002). The position of these structures varies from tens up to thousands of gravitational radii[1], $r_{\rm g} = GM_{\rm BH}/c^2$.

In this framework, and taking advantage of the highly variable behaviour of AGN, detection of time delays, as a function of the Fourier frequency, between the soft band and the hard band photons, can shed light on the X-ray emission mechanism and the geometry of these systems. Currently the observed negative X-ray time-lags (i.e. soft-band variations lagging the hard-band variations; NXTL hereafter), has triggered a great deal of scientific interest on interpreting their nature. After their first tentative detection in the AGN Ark 564 (McHardy et al. 2007), where an origin in reflection from the accretion disc was first proposed, the first statistical significant detection came from Fabian et al. (2009) for the AGN 1H 0707-495. Then, Emmanoulopoulos et al. (2011) found that this time delayed X-ray behaviour is much more common than was initially thought by analysing the data sets from two widely studied bright AGN, MCG–6-30-15 and Mrk 766. Subsequently, De Marco et al. (2013) in a systematic analysis of 32 AGN, found a total of 15 AGN exhibiting NXTLs with high statistical confidence.

The opposite time delayed behaviour i.e. positive X-ray time delays (hard-band variations lag the soft-band variations), has been known for quiet some time in both AGN (e.g. Papadakis et al. 2001; McHardy et al. 2004; Arévalo et al. 2006; Sriram et al. 2009) and X-ray binaries (XRBs; e.g. Miyamoto & Kitamoto 1989; Nowak & Vaughan 1996; Nowak et al. 1999). Although positive time-lags are expected in the standard Comptonisation process within the X-ray source (Nowak et al. 1999), they can also be produced by diffusive propagation of perturbations in the accretion flow (Kotov et al. 2001).

The origin of NXTL still remains unclear. Assuming a lamp-post geometry, in which the reflection of the hard X-rays occurs very close to the BH (few $r_{\rm g}$), the NXTL arise from the difference in the path-lengths between the soft (reflected photons) and the hard X-ray photons (coming directly from the X-ray source) to the observer (Fabian et al. 2009; Zoghbi et al. 2010, 2011; Cackett et al. 2013; Fabian et al. 2013). On the other hand based on the large-scale distant scattering scenario (Miller et al. 2010; Legg et al. 2012), NXTLs might be caused by scattering of X-rays as they pass through, or are scattered from, a distant (tens up to hundred $r_{\rm g}$) absorbing clumpy medium (e.g. wind, outflow, cloud), that partially covers the X-ray source, and whose opacity decreases with increasing energy.

Currently modelling of NXTLs is usually done in terms of simple top-hat impulse response functions (THIRF, hereafter; Miller et al. 2010; Zoghbi et al. 2011; Emmanoulopoulos et al. 2011). This approach is, however, just a parametrisation of the NXTL spectra and does not carry any physical information about the geometry and the physical properties of the BH (i.e. mass, spin). In order to properly model the impulse response function one, one has to take into account in detail the various general relativistic (GR) effects which affect the geometric path of both the hard and reflected X-rays. A first attempt at such a modelling of NXTLs was performed by Chainakun & Young (2012) for the AGN 1H 0707-495 using a GR light-bending model and a moving X-ray source in order to take account of the observed X-ray variability. Their conclusion was that a more complex physical model is required in order to explain both the source's geometry and intrinsic variability. More recently, Wilkins & Fabian (2013) using the full GR treatment with a variety of different geometries of corona, for the same AGN 1H 0707-495, found the the X-ray source extends radially outwards to around 35 $r_{\rm g}$ and at a height of around 2 $r_{\rm g}$ above the plane of the accretion disc and that propagating fluctuations might account for the positive low frequency time delays.

In this paper we perform the first systematic analysis of the time-lag spectra of a sample of 12 AGN using fully general relativistic impulse response functions (GRIRFs, hereafter). These functions are generated using a lamp-post model with variable BH mass, BH spin parameter, viewing angle and height of the X-ray source above the disc. The paper is organised as follows: Initially, in Sect. 2 we present the observations and data reduction procedures. Then, in Sect. 3 we describe the lamp-post model and the method that we use to derive the GRIRFs. In the next section, we outline the procedure for the estimation of the time-lag spectra models from the corresponding GRIRFs, and in Sect. 5 we describe the fitting methodology. Sect. 6 contains the results of the best-fitting time-lag spectral models and finally in the last section we give a summary of our results and we discuss our conclusions. Throughout the paper the error estimates for the various physical parameters correspond to the 68.3 per cent confidence intervals unless otherwise stated. Similarly, the error bars of the plot points in all the figures indicate the 68.3 per cent confidence intervals.

[1] For a BH mass of 2×10^6 M$_\odot$ photons need $t_{\rm g} = r_{\rm g}/c = 9.8$ s to travel a distance of 1 $r_{\rm g}$.

Table 1. *XMM-Newton* observations. The first column, (1), gives the names of the AGN and their BH masses. Each BH mass estimate comes with a footnote (at the end of the table) indicating the corresponding literature reference. Those BH masses that have been estimated using the reverberation mapping technique are followed by the indication (r). The second column, (2), gives the *XMM-Newton* observation IDs together with the corresponding observing mode of the EPIC-pn camera: small window (sw), large window (lw) and full window (fw) mode. The third column, (3), gives the net exposure time of the observations i.e duration after background subtraction and screening.

(1) AGN name BH Mass ($\times 10^6$ $M_\odot$)	(2) Obs ID (PN mode)	(3) Net exp. (ks)
NGC 4395		
0.36 ± 0.11^a (r)	0142830101 (fw)	108.7
NGC 4051		
$1.73^{+0.55}_{-0.52}{}^b$ (r)	0109141401 (sw)	117.0
	0157560101 (lw)	50.0
	0606320101 (sw)	45.3
	0606320201 (sw)	44.4
	0606320301 (sw)	31.3
	0606320401 (sw)	28.8
	0606321301 (sw)	30.1
	0606321401 (sw)	39.2
	0606321501 (sw)	38.8
	0606321601 (sw)	41.5
	0606321701 (sw)	38.3
	0606321801 (sw)	39.9
	0606321901 (sw)	6.2
	0606322001 (sw)	36.9
	0606322101 (sw)	37.7
	0606322201 (sw)	41.1
	0606322301 (sw)	42.3
Mrk 766		
$1.76^{+1.56}_{-1.40}{}^c$ (r)	0304030101 (sw)	95.1
	0109141301 (sw)	128.6
	0304030301 (sw)	98.5
	0304030401 (sw)	98.5
	0304030501 (sw)	95.1
	0304030601 (sw)	98.5
	0304030701 (sw)	34.6
MCG–6-30-15		
2.14 ± 0.36^d	0111570101 (sw)	43.2
	0111570201 (sw)	55.0
	0029740101 (sw)	83.5
	0029740701 (sw)	127.4
	0029740801 (sw)	125.0
Ark 564		
2.32 ± 0.41^e	0006810101 (sw)	10.6
	0206400101 (sw)	98.9
	0670130201 (sw)	59.1
	0670130301 (sw)	55.5
	0670130401 (sw)	62.5
	0670130501 (sw)	66.9
	0670130601 (sw)	60.5
	0670130701 (sw)	55.3
	0670130801 (sw)	57.8
	0670130901 (sw)	55.5
1H 0707-495		
2.34 ± 0.71^f	0110890201 (fw)	40.7
	0148010301 (fw)	78.0
	0506200201 (lw)	38.7
	0506200301 (lw)	38.7
	0506200401 (lw)	40.6
	0506200501 (lw)	40.9
	0511580101 (lw)	121.6
	0511580201 (lw)	102.1
	0511580301 (lw)	104.2
	0511580401 (lw)	101.8
	0554710801 (lw)	96.1
	0653510301 (lw)	113.9
	0653510401 (lw)	125.8
	0653510501 (lw)	117.0
IRAS 13224-3809		
5.75 ± 0.82^f	0110890101 (fw)	60.9
	0673580101 (lw)	126.1
	0673580201 (lw)	125.1
	0673580301 (lw)	125.0
	0673580401 (lw)	127.5
ESO 113-G010		
6.96 ± 0.24^g	0301890101 (fw)	92.6
NGC 7469		
12.2 ± 1.4^h (r)	0112170101 (sw)	17.6
	0112170301 (sw)	23.1
	0207090101 (sw)	84.6
	0207090201 (sw)	78.7
Mrk 335		
26 ± 8^i	0306870101 (sw)	132.8
	0600540501 (fw)	80.7
	0600540601 (fw)	130.3
NGC 3516		
$31.7^{+2.8}_{-4.2}{}^b$ (r)	0107460601 (sw)	79.3
	0107460701 (sw)	120.5
	0401210401 (sw)	51.7
	0401210501 (sw)	62.6
	0401210601 (sw)	61.6
	0401211001 (sw)	42.2
NGC 5548		
$44.2^{+9.9}_{-13.8}{}^b$ (r)	0089960301 (sw)	85.2

[a] Peterson et al. (2005)
[b] Denney et al. (2010)
[c] Bentz et al. (2009)
[d] Estimated from equation 3 in Gültekin et al. (2009) using the stellar velocity dispersion value of McHardy et al. (2005).
[e] Estimated from equation 5 in Vestergaard & Peterson (2006) using the mean values of FWHM(H_β) and λL_λ(5100 Å) of Romano et al. (2004).
[f] Zhou & Wang (2005)
[g] Estimated from equation 5 in Vestergaard & Peterson (2006) using the mean values of FWHM(H_β) and the λL_λ(5100 Å) estimated by Cackett et al. (2013) using data of Pietsch et al. (1998).
[h] Peterson et al. (2004)
[i] Grier et al. (2012)

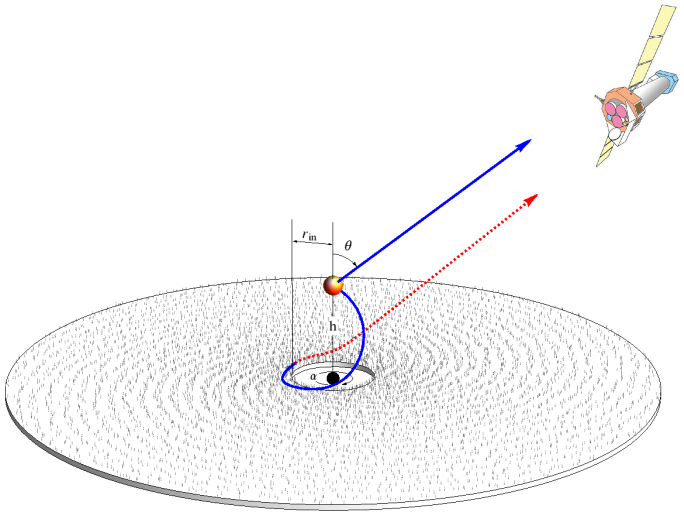

Figure 1. Geometrical layout of the lamp-post geometrical model. The accretion disc is an optically thick, geometrically thin, Keplerian cold (i.e. neutral) disc that extends from the ISCO, $r_{\rm in}$, which is defined by the BH spin parameter, α, to 1000 $r_{\rm g}$. The X-ray source is depicted by the orange sphere and it is situated at a height h above the BH. The blue solid lines correspond to the trajectories of two example hard X-ray photons leaving the X-ray source, one heading towards the observer and another one towards the accretion disc. The latter follows a curved trajectory, due to the GR effects, and the trajectory of the corresponding soft X-ray photon from the accretion disc (reflected product) is shown with the red dotted line. The whole system is viewed from an angle θ. –A colour version of this figure is available in the online version of the journal–

2 OBSERVATIONS AND DATA REDUCTION

In Table 1 we list the details of the *XMM-Newton* observations which we used in this work. In the second column we list the Observation ID for each object. The letters in parenthesis refer to the pn observation mode; fw, lw, and sw refer to the `PrimeFullWindow`, `PrimeLargeWindow` and `PrimeSmallWindow` modes, respectively.

The *XMM-Newton* data were processed using SCIENTIFIC ANALYSIS SYSTEM (SAS) (Gabriel et al. 2004) version 12.0.1. We consider only the EPIC pn data (Strüder et al. 2001) as they have a higher count rate and lower pile-up distortion than the MOS data. The source counts for each AGN were accumulated from a circular aperture of radius 40″ centered on the source. The background counts were accumulated from a source-free circular region on the same CCD chip as the source. For the type of events, we selected only single and double pixel events, i.e. `PATTERN==0-4`, and we rejected bad pixels and events too close to the edges of the CCD by using the standard quality criterion `FLAG==0`.

Source and background light curves were extracted using `evselect` in 10 s time bins. We checked all light curves for pile-up using the task `epatplot`. We found that only three observations of Ark 564 were affected by moderate pile-up with Obs. IDs: 0670130201, 0670130501 and 0670130901. In these cases, we used an annular region to exclude the innermost source emission having a radius, in pixels, of: 280, 200 and 250, respectively. The source light curves were screened for high background and flaring activity. The light curve parts with high background activity, usually at the beginning and/or end of an observation, were removed from the final data products. The total on-source `pn` exposure time, as well as the net exposure time after the exclusion of the high background activity periods, are listed in the third column of Table 1.

Since we are interested in studying the time-lags between the soft excess and the X-ray continuum, the source and background light curves were extracted in those energy bands where the soft excess contribution is maximized and the continuum emission is dominating, respectively. Thus, for all the sources, we use for the soft excess and the continuum the energy bands of 0.3–1 and 1.5–4 keV, respectively. The background subtracted light curves were produced using `epiclccorr`. Note that in Sect. 4.2.1 we discuss why for the purposes of our paper is not necessary detailed fine-tuning of the selected energy bands.

The resulting data sets are continuously sampled suffering only from very few data gaps and count rate drops (as a consequence of telemetry drop-outs). With respect to the data gaps, on average there are at most 3–6 missing observations which we filled up by linear interpolation. For the count rate drops, that are also very few (on average between 2–5 points), we rescale the count rate within the each bin according to the corresponding fractional exposure time.

3 THE LAMP-POST MODEL

In this section we describe the basic physical and geometrical properties of the lamp-post model. Then, we outline the process that we use to estimate the GRIRFs. All the time scales are estimated in normalised time units, of $t_{\rm g}$, and thus they scale linearly with M via the relation

$$t_{{\rm g},M} = 4.9255M \text{ s} \quad (1)$$

where M is the BH mass given in units of 10^6 $M_\odot$.

3.1 The geometrical layout and parameter space

The lamp-post model that we consider in this paper consists of the following three physical components: a central supermassive BH with an accretion disc illuminated by a point-like X-ray source located on the axis of the system (Fig. 1). The system is characterised by the following parameters: spin parameter and mass of the central BH, height of the X-ray source, and viewing angle of the system.

The accretion disc extends from the inner most stable circular orbit (ISCO=$r_{\rm in}$) to 1000 $r_{\rm g}$ and it is an optically thick, geometrically thin, Keplerian cold (i.e. neutral) disc. The X-ray source lies above the BH at height h and it comprises the primary source of X-rays, which we assume to be static and to be emitting isotropically with a power-law spectrum of photon index $\Gamma = 2$.

The central BH is characterised by its spin parameter, α, and its mass, M. For the former, which defines the ISCO, we consider three values: 0 (Schwarzschild BH, $r_{\rm in} = 6\ r_{\rm g}$), 0.676 (intermediate spin BH, $r_{\rm in} = 3.5\ r_{\rm g}$) and 1 (maximally rotating Kerr BH, $r_{\rm in} = 1\ r_{\rm g}$).

We have chosen a variety of heights for the X-ray source depending on the spin of the BH. For the case of a Schwarzschild BH we select an ensemble of 18 heights: $\{2.3, 2.9, 3.6, 4.5, 5.7, 7, 8.8, 11, 13.7, 17.1, 21.3, 26.5, 33.1, 41.3, 51.5, 64.3, 80.2, 100\}\ r_{\rm g}$. For the intermediate case we add to the ensemble a lower height of 1.9 $r_{\rm g}$, and for the Kerr BH we add yet another height of 1.5 $r_{\rm g}$, respectively.

Finally, the system is observed by a distant observer at an viewing angle of θ i.e. $\theta = 0$ or 90° if the disc is phase on or edge on, respectively. For each one of the three BH spin parameters and each one height we consider three angles: 20 40 and 60°.

This wide parameter space, consisting of the variables α, h and θ, yields a total of $(20+19+18)\times 3 = 171$ different geometrical layouts of the lamp-post model. The BH mass is not an additional variable in our estimation of GRIRFs as all time-scales and frequencies scale linearly with it (equation 1). In each geometry the photons will follow different trajectories from the X-ray source to the disc and from the disc to the observer and thus the response of the system will be different.

3.2 Estimation of the GRIRFs

In order to compute the response of the accretion disc to the primary illumination from the X-ray source (described by the power-law) we use a flare with a step function profile that has very short duration of 1 $t_{\rm g}$. The primary intrinsic spectrum has a normalisation of unity. Then we estimate the response of the disc by measuring the flux *only* of the neutral fluorescent Fe Kα line, at 6.4 keV in the rest frame of the accretion disc.

To compute the Fe Kα line flux we use NOAR (Dumont et al. 2000) consisting of a Monte-Carlo method that takes into account both the direct and inverse Compton scattering processes. We assume an abundance equal to the Solar one and a neutral accretion disc. The resultant flux at the observer is computed using all the general relativistic effects (Dovčiak et al. 2004) without taking into account higher order images of the disc. Thus we exclude the photons emitted from the accretion disc (either from the top or the bottom surface) that go around the BH close to the photon orbit (any number of times) and still should arrive to the observer passing through the region below ISCO. Higher order images are more prominent for a Schwarzshild BH where the ISCO is the furthest out and the gap between the inner edge of the disc and the BH is the largest. Nevertheless even in this case these do not contribute very much to the total flux (Beckwith & Done 2004).

The GR effects include the light bending that causes the gravitational lensing, energy shift – Doppler and gravitational, and the relativistic time delays for both the photons travelling from the primary source to the disc as well as the re-processed photons emitted from the disc and travelling towards the observer. Due to the lamp-post geometry and relativistic effects, the illumination of the accretion disc from the primary X-ray source is uneven (i.e. depending on the radius). The reflected flux from the disc is proportional to the incident flux on the disc which is a power-law with its normalisation being a function of α, h, θ and Γ (see equation 3 in Dovčiak et al. 2011).

Due to the GR effects, the flux of the Fe Kα line is spread over a wide range of energies as a function of time yielding for each lamp-post configuration a *dynamic reflection spectrum*, estimated with a time resolution of 0.1 $t_{\rm g}$[2]. In the left-hand panel of Fig. 2 we show an example of a Fe Kα dynamic reflection spectrum for the case of $\alpha = 0.676$, $\theta = 40°$ and $h = 3.6\ r_{\rm g}$. As we can see the flux of the Fe Kα line is spread over a wide range of energies between 2.5–7 keV and fades-out as time goes on, indicating the decay of the 'echo' as it is moving away from the centre of the accretion disc.

In order to derive the GRIRF, $\Psi(t)$, of the accretion disc for the Fe Kα emission line we use the dynamic reflection spectra and we add up for a given time all the Fe Kα line fluxes in the energy band 0–8 keV. In the right-hand panel of Fig. 2 we show the GRIRF which corresponds to the dynamic reflection spectrum of the left-hand panel. This plot in effect shows how the Fe Kα line flux (in 0–8 keV) evolves with time, as seen by a distant observer. The actual sums are depicted by the black points and the dotted line is a cubic interpolation. Note that the cubic interpolation is needed because in some cases there are very small numerical errors during the estimation of the line flux in the dynamic spectra (of the order of 10^{-5}) which can create oscillatory artefacts (Fig.3) in the corresponding GRIRF (during the summation process). By performing a cubic interpolation (as opposed to a linear or quadratic) these artefacts are suppressed and the integration process which is used to derive the time-lag spectra (Sect. 4.1) is much faster (i.e. there is no need to take globally a very small integration step).

As we can see from the right-hand panel of Fig.2, the general shape of the IRFs consists of an abrupt rise followed by two peaks and a decay. The onset of the first peak corresponds to the time that the first hard X-ray photons hit the disc and from that point, a ring of expanding echo is created.

[2] Sometimes the dynamic reflection spectrum is called '2D transfer function' (Campana & Stella 1995; Reynolds et al. 1999) despite the fact that that strictly speaking in signal processing the term 'transfer function' refers to the Fourier domain i.e. ratio of the Fourier transformed input to output signals.

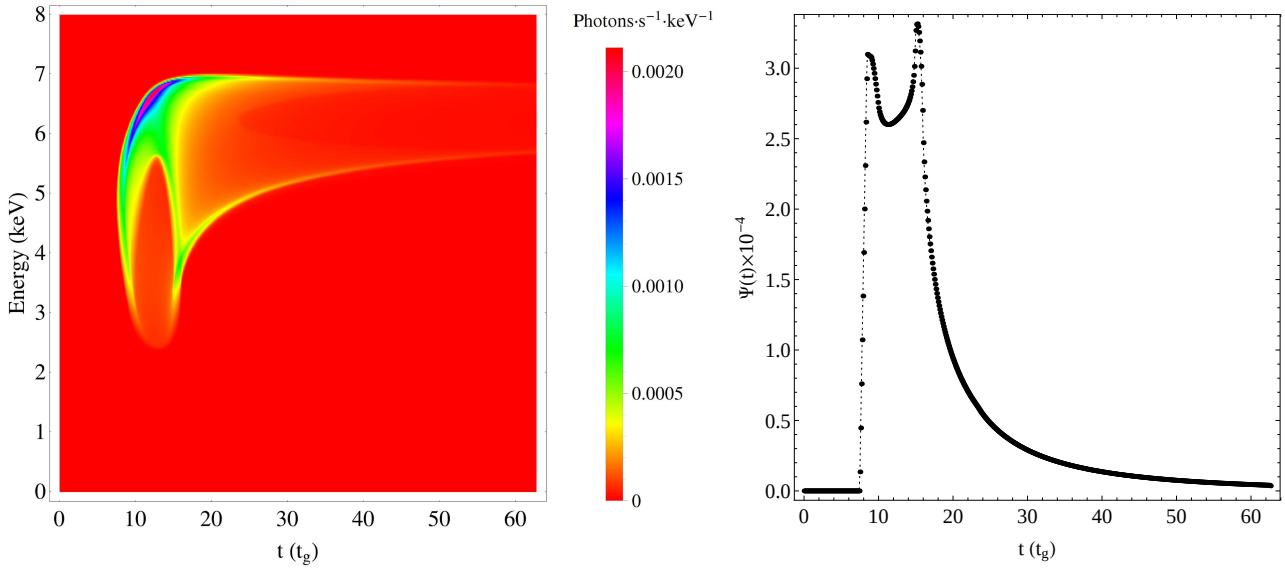

Figure 2. Estimation of the GRIRF for the lamp-post model with $\alpha = 0.676$, $\theta = 40°$ and $h = 3.6\ r_{\rm g}$. Left-hand panel: The dynamic reflection spectrum with a time resolution of 0.1 $t_{\rm g}$. –A colour version of this figure is available in the online version of the journal– Right-hand panel: The GRIRF derived by adding up the Fe Kα line flux at a given time (black points) and the dotted line is a cubic interpolation.

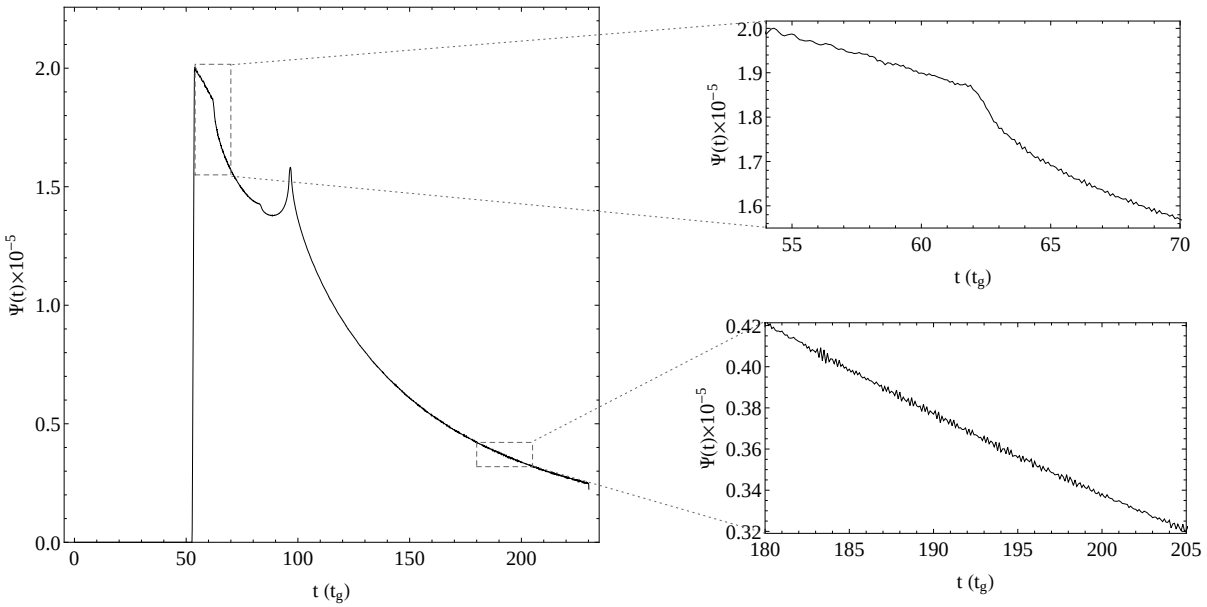

Figure 3. Small scale oscillatory artefacts. The plot shows the linearly interpolated GRIRF for the lamp-post model with $\alpha = 0$, $\theta = 60°$ and $h = 51.5\ r_{\rm g}$. The dashed rectangles zoom in two regions of the GRIRF where the oscillatory artefacts are prominent.

As the part of the echo approaches the BH it is deformed in such a way that eventually two echoes are created, inner and outer, which correspond to the second peak in the IRF. The inner ring is then moving towards the BH, the outer one continues with its radial expansion away from the centre of the disc and the IRF is gradually fading out. For low spin values (e.g. for the Schwarzschild BH) the inner ring is not created due to the existence of the hole in the accretion disc below the ISCO. The second peak in the transfer function in this case corresponds to the re-appearance of the part of the outer ring behind the BH after it was 'hidden' below the ISCO.

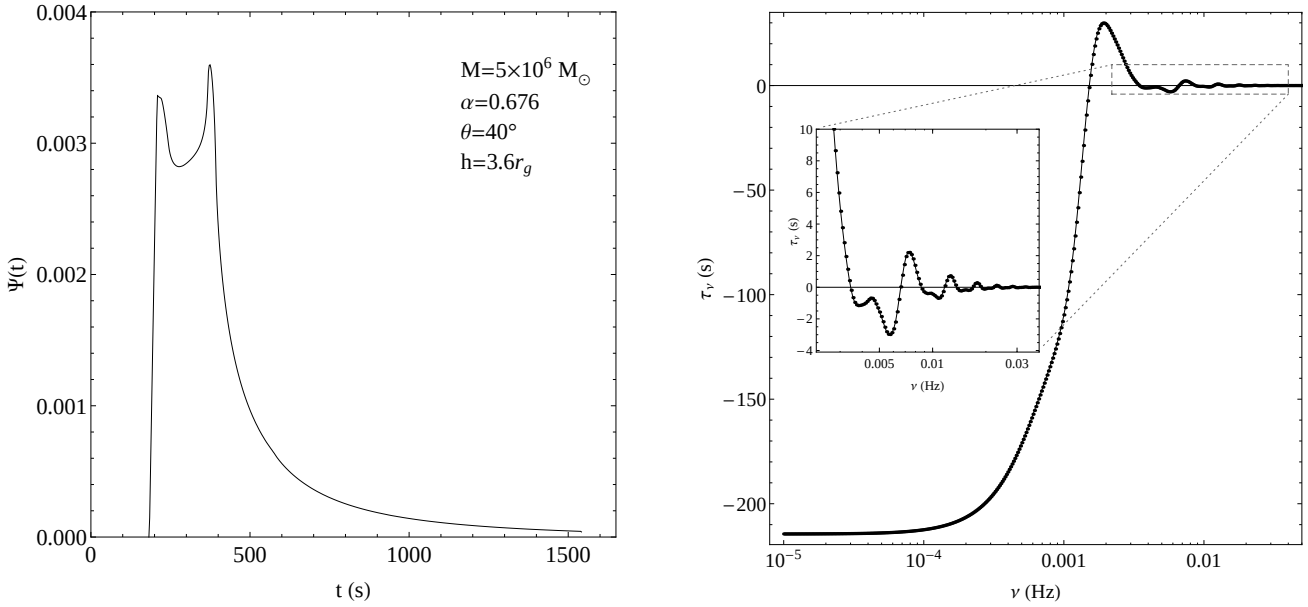

Figure 4. Estimation of time-lag spectrum for the lamp-post model with $\alpha = 0.676$, $\theta = 40°$ and $h = 3.6\ r_{\rm g}$, for $M = 5 \times 10^6\ {\rm M}_\odot$. Left-hand panel: The GRIRF model in physical units (a scaled version of Fig. 2, right-hand panel). Right-hand panel: The corresponding time-lag spectrum.

4 TIME-LAG SPECTRA ESTIMATION

4.1 Model time-lag spectra

We can now use the GRIRFs that we have computed for the iron line photons, to construct model time-lag spectra as follows. Assume that the X-ray spectrum of AGN can be described by a power-law form $a(t)E^{-\Gamma}$, where Γ is a constant as a function of time and all the observed flux variability is due to the variations of the normalization $a(t)$ (primary continuum). Then, the source's hard X-ray emission in the 1.5–4 keV band, $h(t)$, which is dominated by the X-ray continuum source can be written as

$$h(t) = ba(t) \tag{2}$$

where $b = \int_{1.5\ {\rm keV}}^{4\ {\rm keV}} E^{-\Gamma} dE$. Let's then assume that $s(t)$ is the variable source's soft X-ray emission in the 0.3–1 keV energy range where, in addition to the continuum, we also detect emission from the reprocessing component so that

$$s(t) = ka(t) + f \int_0^\infty \Psi(t')a(t-t')dt' \tag{3}$$

where $k = \int_{0.3\ {\rm keV}}^{1\ {\rm keV}} E^{-\Gamma} dE$, and $\Psi(t')$ are the GRIRFs for the iron line photons over the 0–8 keV band that we discussed in the previous section (Sect. 3.2).

In this way, we basically assume that the photons of the reflected component which contribute to the observed 0.3–1 keV band and the iron line photons at 6.4 keV are produced in the same parts of the disc, hence the shape of the soft band GRIRF is similar to the GRIRFs that we have estimated for the iron line photons. However, even if this is the case, we do not expect the flux of the soft-band reflection spectrum to be the same as the iron line flux (i.e. difference in the normalisation), hence the use of the constant f in the above equation.

In order to derive the time-lag spectrum between the $s(t)$ and $h(t)$ bands we need to estimate the cross-covariance function between the two time series. This function at a time-lag τ is defined as:

$$r_{s,h}(\tau) = {\rm E}\left[(s(t) - \langle s(t)\rangle)\,(h(t+\tau) - \langle h(t)\rangle)\right] \tag{4}$$

where E is the expectation operator, and the values in brackets denote mean values. It can be shown that in our case,

$$r_{s,h}(\tau) = bkr_{a,a}(\tau) + fb \int_0^\infty \Psi(t') r_{a,a}(\tau + t')dt' \tag{5}$$

where $r_{a,a}(\tau)$ is the auto-covariance function of the continuum variability process,

$$r_{a,a} = E\left[(a(t) - \langle a(t)\rangle)\,(a(t+\tau) - \langle a(t)\rangle)\right] \tag{6}$$

If we take the Fourier transform of both sides of the above equation, we obtain

$$\mathscr{P}_{s,h}(\nu) = bk\mathscr{P}_{a,a}(\nu)[1 + (f/k)\int_0^\infty \Psi(t') e^{-i2\pi\nu t'} dt'] \tag{7}$$

where $\mathscr{P}_{s,h}(\nu)$ is the cross-spectral density function between $h(t)$ (i.e. the input X-ray emission) and $s(t)$ (i.e. the output reflected emission) at frequency ν, and $\mathscr{P}_{a,a}(\nu)$ is the power spectral density function of the continuum. The function $\mathscr{P}_{s,h}(\nu)$ is a complex function, and its complex argument defines its phase, at frequency ν, i.e. the phase-lag between the time series $s(t)$ and $h(t)$. Since $\mathscr{P}_{a,a}(\nu)$ is a real function, equation 7 implies that the time-lag, $\tau(\nu)$, between the two time series at frequency ν is given by

$$\tau_\nu = -\frac{\arg\left[1 + (f/k)\int_0^\infty \Psi(t') e^{i2\pi\nu t'} dt'\right]}{2\pi\nu} \tag{8}$$

We use equation 8 to estimate the model time-lag spectra for each one of the model GRIRF (in total 171, Sect. 3) . For each $\Psi(t')$, the integral in this equation

was estimated at 491 frequencies: $\nu = 10^k$ Hz with $k = -5, -4.99, \ldots, -0.11, -1$. These frequencies cover the typical frequency range covered by *XMM-Newton*. Note that for the integration procedure we use adaptive integration method which identifies the problematic integration areas, which in our case are usually the regions of the two peaks, and concentrate the computational effort (i.e. sampling points) on them (Malcolm & Simpson 1975; Krommer & Ueberhuber 1998). The resulting model time-lag model spectrum have an almost continuous profile, due to the very fine frequency resolution we have adopted. Therefore, this allows us to interpolate linearly among the various frequencies without adding additional structure into the resulting time-lag spectra.

The resulting time-lag spectra originate from equation 8 which contains the integral of the GRIRF, $\Psi(\tau')$, in normalised time units (i.e. $t_{\rm g}$). Thus, if one wants to work in conjunction with real data (e.g. for fitting purposes, as we are doing in Sect. 6) then one has to transform the time-lag spectra into real physical units (i.e. seconds) by dividing and multiplying the abscissas (frequencies, ν) and the ordinates (time-lag estimates, τ_ν) respectively by $t_{{\rm g},M}$ (equation 1).

For demonstrative purposes in the left-hand panel of Fig. 4 we show the GRIRF in physical time units for a BH mass of 5×10^6 M$_\odot$ corresponding to the GRIRF shown in normalised units in the right-hand panel of Fig. 2 ($\alpha = 0.676$, $\theta = 40^\circ$ and $h = 3.6$ $r_{\rm g}$). The corresponding time-lag spectrum for this GR reflection scenario is in general a negative function (Fig. 4, right-hand panel). The first morphological characteristic of this time-lag spectrum is that at low frequencies, $10^{-5}-10^{-4}$ Hz (i.e. long time scales) it exhibits a negative tail that forms a constant plateau -215 s. This plateau defines the most negative time delayed reflected emission from the disc (i.e. its ordinate) and the corresponding time scales that these delays occur (i.e. 10–100 ks). Then, the values of the time-lag spectrum increase as a function of frequency and they become positive at 1.5×10^{-3} Hz, peaking around (2×10^{-3} Hz, 30 s). Finally, the time-lag spectra exhibit a damped oscillating behaviour (Fig. 4, inset) around zero.

In general, all the time-lag spectra exhibit these features but they appear at different frequencies depending on the BH mass, the height of the X-ray source and r_{min}. Note, that whether the time-lag values become positive or remain always on a negative level depends only on the shape of corresponding GRIRF (as shown in equation 8). In Appendix A1 we explore the model parameter space for different configurations of the lamp-post model.

4.1.1 GRIRF vesrus THIRF

In this section we compare the physically justified GRIRFs with the widely used (see for references Sect. 1) THIRF parametrisation model. We employ the case of the lamp-post model with the following parameters: $\alpha = 1$, $\theta = 40^\circ$ and $h = 26.5$ $r_{\rm g}$, for a for a BH mass $M = 2 \times 10^6$ M$_\odot$. For this case, the GRIRF is shown in the left-hand panel of Fig.5 with the black line. Then we consider two top-hat parametrisation scenarios (both of them normalised to unity) to represent the given GRIRF: one with width defined to be equal to the separation of the two peaks in the real GRIRF (Top-hat 1, Fig.5, left-hand panel, dotted thick grey line) and the other one starting at the same time as the real GRIRF and extending over the full time range covered by it (Top-hat 2, Fig.5, left-hand panel, solid thick grey line). As we can see from the right-hand panel of Fig.5, the corresponding time-lag spectra of the two THIRFs differ genuinely from that of the GRIRF. The position of the negative constant plateau, the position and the amplitude of the first positive peak as well as the behaviour is high frequencies (above 10^{-3} Hz) differ significantly from those in the time-lag spectrum of the GRIRF. Note that similar discrepancies occur for lower heights of the X-ray source.

The top-hat parametrisation yields always two numbers: the start- and the end-time of the rectangular pulse. In both scenarios that we have considered, the start-time is associated with the beginning of the reverberation phenomenon on the accretion disc (first peak of the GRIRF) i.e. the time that the first hard X-ray photons hit the disc, which is a physically real parameter of the system. The end-time could correspond either to the second peak of the GRIRF where the iso-delayed arcs (travelling opposite and around the BH) meet for the first time, (Top-hat 1) or to the overall time of the reverberation phenomenon (Top-hat 2) (see Sect. 3.2 for the various peaks and times of the GRIRF). However, none of these scenarios yield a time-lag that matches that of GRIRF.

Finally, in order to retrieve the best-fitting THIRF model, that could correspond to the time-lag spectrum of the given lamp-post geometry, we fit to the time-lag spectral estimates (shown in Fig.5, right-hand panel, black line) equation 8, using as $\Psi(\tau)$ a top-hat function leaving as free parameters τ_1' and τ_2' (i.e. start and end-times) under the condition $\tau_1' < \tau_2'$ (e.g. Zoghbi et al. 2011; Emmanoulopoulos et al. 2011). This is done by finding the pair $\{\tau_1', \tau_2'\}$ that minimises the squared sum of the distance of between the two functions estimated over th 491 frequencies points of the time-lag spectrum (Sect. 4.2).

The best-fitting THIRF model is shown in the left-hand panel of Fig.6 with the with the thick grey line together with the physically realistic GRIRF model (black line). The quality of the fit is poor (squared sum equals to 188288 s^2 for 489 degrees of freedom, –d.o.f.–), but more importantly, the best-fitting THIRF has physically unrealistic times $\{\tau_1', \tau_2'\} = \{-4545, 3108\}$ s that can not be associated with any time-scale of the system[3]. As we can see, the from the right-hand panel of Fig.6, the top-hat model, that corresponds to the best-fitting times (thick, grey line), covers completely different time-scales from the GRIRF model (black- line) and thus can not be associated with any genuine physical property of the system.

4.2 Observed time-lag spectra

In order to estimate the time-lag spectra between two light curves we use we use the standard analysis method outlined in Bendat & Piersol (1986); Nowak et al. (1999). In brief, consider for a given source a soft and a hard light curve, $s(t)$

[3] Constraining the problem only to the positive domain i.e. $0 < \tau_1' < \tau_2'$ yields practically a zero width best-fitting THIRF with $\{\tau_1', \tau_2'\} = \{1.1, 1.3\} \times 10^{-5}$ s, having a very poor fit characterised by a squared sum of 2.12×10^7 s^2 for 489 d.o.f.

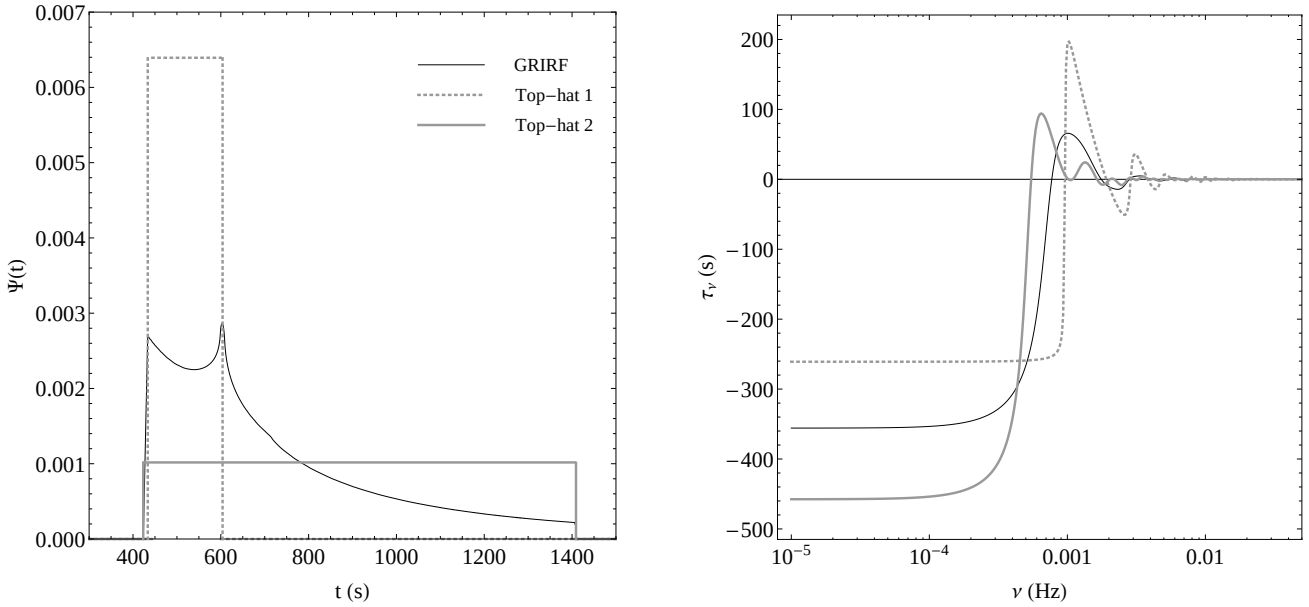

Figure 5. GRIRF versus THIRF for the lamp-post model with $\alpha = 1$, $\theta = 40^\circ$ and $h = 26.5\ r_{\rm g}$, for $M = 2 \times 10^6\ {\rm M}_\odot$. Left-hand panel: The GRIRF (black line) and the two top-hat parametrisation models each one depicting the two peaks (dotted thick grey line) and the overall shape (solid thick grey line) of the GRIRF, respectively. Right-hand panel: The corresponding time-lag spectra.

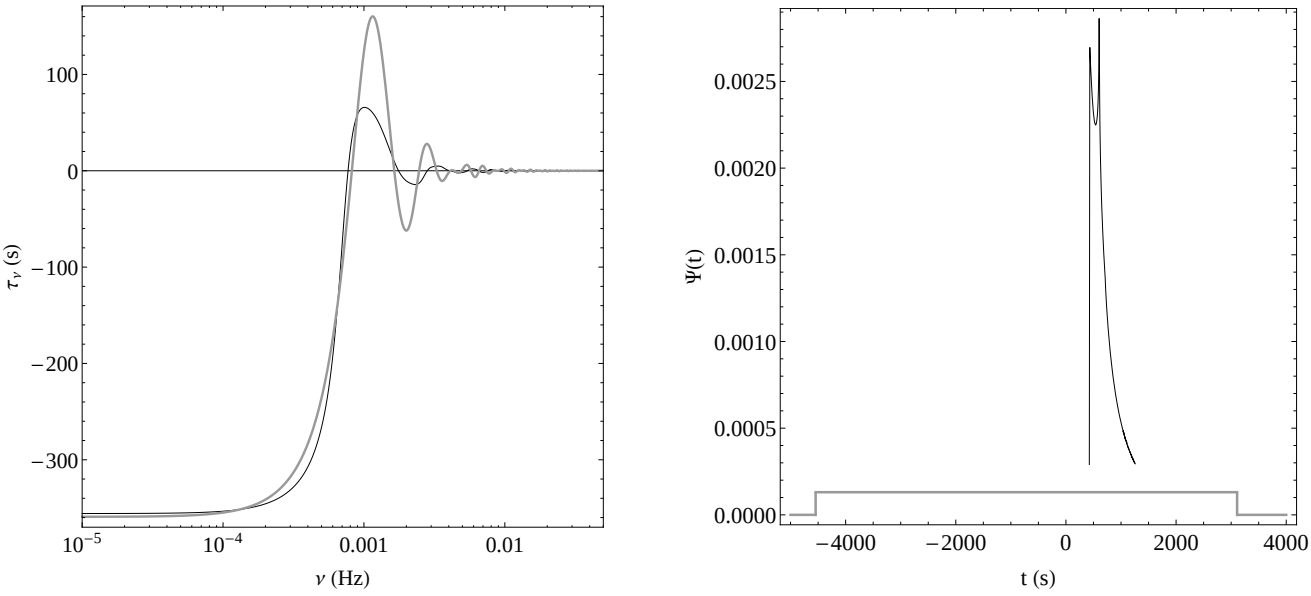

Figure 6. Fitting the time-lag spectrum of the lamp-post model with $\alpha = 1$, $\theta = 40^\circ$ and $h = 26.5\ r_{\rm g}$, for $M = 2 \times 10^6\ {\rm M}_\odot$with a time-lag spectrum coming from a THIRF. Left-hand panel: The best-fitting time-lag spectrum (thick, grey line), for $\{\tau_1', \tau_2'\} = \{-4545, 3108\}$ s, and the lamp-post time-lag spectrum (black line, also shown in the right-hand panel of Fig. 5). Right-hand panel: The corresponding THIRF, derived from the best-fitting parameters, (thick, grey line) together with the GRIRF of the lamp-post model (black line, also shown in the left-hand panel of Fig. 5).

and $h(t)$, obtained simultaneously, consisting of the same number of N equidistant observations with a sampling period $t_{\rm bin}$ (these are discretized and finite length versions of equations 3 and 2, respectively). For a given Fourier frequency, $f_j = j/(Nt_{\rm bin})$ for $j = 1, 2, \ldots, [N/2$ or $({\rm N}-1)/2]$ (for even or odd N) we estimate the cross-spectrum, $\mathscr{C}(f_j)$[4], (e.g. Priestley 1981) between the two light curves in a phasor

[4] This is a natural estimator of the continuous cross-spectrum equation 7.

form as

$$\mathscr{C}_{s,h}(f_j) = S^*(f_j)H(f_j) = |S(f_j)||H(f_j)|e^{i\left(\phi_H(f_j)-\phi_S(f_j)\right)} \quad (9)$$

in which $S(f_j)$ and $T(f_j)$ are the discrete Fourier transforms of $s(t)$ and $y(t)$, respectively, with phases $\phi_S(f_j)$ and $\phi_H(f_j)$ and amplitudes $|S(f_j)|$ and $|H(f_j)|$, respectively. The asterisk denotes complex conjugation.

Then, we average the complex cross-spectrum estimates over a number of of at least 10 consecutive frequency bins, $f_{\mathrm{bin},i}$ for $i = 1, 2, \ldots, m$, yielding m average cross-spectra estimates, $\langle\mathscr{C}_{s,h}(f_{\mathrm{bin},i})\rangle$. Finally, for each average cross spectrum we derive its complex argument i.e. its angle with the positive real axis, known also as *phase*, $\phi(f_{\mathrm{bin},i})$ and we convert it to physical time units

$$\tau(f_{\mathrm{bin},i}) = \frac{\phi(f_{\mathrm{bin},i})}{2\pi f_{\mathrm{bin},i}} \quad (10)$$

For each time-lag estimate we calculate the corresponding standard deviation, std$\{\tau(f_{\mathrm{bin},i})\}$ via equation 16 in Bendat & Piersol (1986).

At the same time from the cross-spectrum we estimate the coherence between $s(t)$ and $h(t)$ as a function of Fourier frequency (Vaughan & Nowak 1997)

$$\gamma_{s,h}(f_j) = \frac{|\langle\mathscr{C}_{s,h}(f_j)|\rangle^2}{\langle|S(f_j)|^2\rangle\langle|H(f_j)|^2\rangle} \quad (11)$$

that takes values between 0 and 1 and it is a measure of the linear correlation between the two light curves at a given Fourier frequency. A very important cautionary point is that small coherence values correspond to uncorrelated phases, $\phi_S(f_j)$ and $\phi_H(f_j)$, whose differences are actually depicted by the $\phi(f_{\mathrm{bin},i})$ (averaged over a range of frequencies). Thus, for uncorrelated phases, $\phi(f_{\mathrm{bin},i})$ has a rather uniform distribution in the range $(-\pi, \pi]$ (due to phase-wrapping) that averages always to zero. That means that for small coherence values we get a time-lag of 0 that has small uncertainties, due to the large number of averaging points, appearing statistical meaningful even if there is not a real correlation between the phases and hence no meaningful time delay.

In all our analysis we estimate the time-lag spectra down to $(3-5)\times10^{-3}$ Hz, but for the fitting procedure we consider only the time-lag estimates for which the coherence is greater that 0.15 corresponding to a physically meaningful phase correlation.

4.2.1 Selection of energy bands

As we discussed in Sect. 2 for all the sources we extracted the light curves between 0.3–1 (soft band) and 1.5–4 (hard band) keV energy bands and these are the ones that we use for the extraction of the time-lag spectra. These bands depict quiet accurately the general behaviour of the reflection component (i.e. soft excess) and that of the X-ray source (i.e. continuum) despite the fact that for each source separately the exact limits could be shifted slightly towards higher or lower energies.

However, for the purposes of this paper we are not so much interested to fine-tune the corresponding soft and hard energy bands since the GRIRF that we use in the first place for our modelling correspond to the response of the neutral Fe Kα line at 6.4 keV (Sect. 3.2) and not the response of the soft excess region in a given source. Thus, the selected energy bands offer us a simple homogeneous description of both the soft and the hard behaviour for the ensemble of sources.

5 THE FITTING PROCEDURE

In order to fit the observed time-lag spectra, $\tau(f_{\mathrm{bin},i})$ binned into m frequency bins (Sect. 4.2), we require two time-lag spectral model components. The first one corresponds to the GR reflected component, estimated from equation 8 for a given GRIRF. This component, carries all the physical and geometrical information about the lamp-post model and gives rise predominantly to negative lags, particularly at the low frequency range. In total we have 171 these negative time-lag spectral models, $\tau_\nu(M, \alpha, \theta, h)$, (each one corresponding to a different set of $\{\alpha, \theta, h\}$ lamp-post model parameters for a given M) estimated for the ensemble of GRIRFs (Sect. 4.1). In principle, the constant f (appearing in equation 8) should be left as a free model parameter. However, given the complexity of the model fitting (as explained below), this would result in a prohibitively large number of model spectra to compare to a limited number of observed points for each object. For this reason, we fix f to 0.3, so that the total emission flux of the Fe Kα line, over all energies, is 30 per cent that of the input X-ray continuum spectral flux. This is in rough agreement to the observed flux ratio between the reprocessing component flux over the continuum flux at soft energies (e.g. Crummy et al. 2006). The second component consists of a simple power-law, $PL_\nu(A, s) = A\nu^{-s}$, providing us with positive time-lags. Thus, we deal with a five-dimensional model parameter space consisting of model parameter vectors of the form, $\mathbf{v} = \{M, \alpha, \theta, h, A, s\}$.

In this framework, the overall time-lag spectral model at a given frequency, ν, is given by the sum of the two components

$$TL_\nu(\mathbf{v}) = \tau_\nu(M, \alpha, \theta, h) + PL_\nu(A, s) \quad (12)$$

Then we transform each one of the 171 GR reflected model components into physical time units (using equation 1)) for an ensemble of 12 BH masses: $(0.01, 0.05, 0.1, 0.5, 1, 2, 5, 10, 50, 100, 200, 500) \times 10^6$ M$_\odot$, yielding a grid of 2052 cells each one corresponding to a given set of parameter values $\{M, \alpha, \theta, h\}$. For each grid-cell we treat the model (i.e. equation 12) in exactly the same way as the observed time-lag spectra i.e. we discretize it and average it over exactly the same number of frequency bins. This yields for each frequency, $f_{\mathrm{bin},i}$, an average value of the overall time-lag model, $\left\langle TL_{f_{\mathrm{bin},i}}(\mathbf{v})\right\rangle$ for $i = 1, 2, \ldots, m$.

For demonstrative purposes, in Fig.7 we show the effects of the discretization and averaging on the continuous time-lag model $TL_\nu(2\times10^6$ M$_\odot, 0.676, 20^\circ, 33.1$ $r_\mathrm{g}, 0.2$ s$, 0.8)$ and on its two components. For the discretization we assume an observational data set of 80 ks binned in 100 s, yielding 400 model estimates at Fourier frequencies between $(1.25\times10^{-5} - 5\times10^{-3})$ Hz separated by 1.25×10^{-5} Hz. Then, these binned model estimates are averaged over 16 frequency bins whose overall range is shown with the horizontal line. The left-hand panel of Fig.7 shows the GR reflected component, $\tau_\nu(2\times10^6$ M$_\odot, 0.676, 20^\circ, 33.1$ $r_\mathrm{g})$, exhibiting in the continuous version a great deal of 'oscillatory-structures' towards high frequencies $(4\times10^{-3} - 2\times10^{-2})$

Hz which are suppressed during the averaging process. The middle-panel of Fig.7 shows the power-law model component, $PL_{\nu}(0.2\ \mathrm{s}, 0.8)$, in which once again the discrete estimates differ from the actual continuous power-law model estimates, at the corresponding frequencies, due to the averaging process. The most prominent differences are at the first frequency bins, particularly the first one at 10^{-4} Hz. Finally, the right-hand panel of Fig.7 shows the overall time-lag model, i.e. the sum of the previous two model components. The discrete averaged version of the overall time-lag model carries all the previously mentioned differences with respect to its continuous version.

Then for each averaged discretized overall time-lag spectral model, within each grid-cell, k, we estimate practically the squared differences between the model and the data using the following χ^2 indicator

$$\chi^2_k(\mathbf{v}) = \sum_{i=1}^{m} \frac{\left(\left\langle TL_{f_{\mathrm{bin},i}}(\mathbf{v})\right\rangle - \tau(f_{\mathrm{bin},i})\right)^2}{\mathrm{std}\{\tau(f_{\mathrm{bin},i})\}^2} \quad (13)$$

and for each grid-cell we minimise this quantity with respect to the two power-law model parameters, $\{A, s\}$. Finally, we end up with an ensemble of 2052 global minimum values of $\chi^2_k(\mathbf{v})$ from which the smallest one corresponds to the set of the best-fitting grid model parameter values $\mathbf{v}_{\mathrm{gbf}} = \{M_{\mathrm{gbf}}, \alpha_{\mathrm{gbf}}, \theta_{\mathrm{gbf}}, h_{\mathrm{gb}}, A_{\mathrm{gbf}}, s_{\mathrm{gbf}}\}$. For the minimisation we use the the classical Levenberg-Marquardt method (Bevington & Robinson 1992).

After localising the $\mathbf{v}_{\mathrm{gbf}}$ we estimate the 68.3 per cent confidence bands for the best-fitting model parameters in the usual way i.e. by varying its value over a given range and deriving each time for the rest model parameters their best-fitting value that yield a $\Delta\chi^2 = 1$ from the minimum $\chi^2_k(\mathbf{v}_{\mathrm{gbf}})$. During the error estimation process we cubically interpolate the $\chi^2_k(\mathbf{v})$ space around its BF best-fitting grid parameter values in the following way: two BH mass cells above and below M_{gbf}, three height cells above and below h_{gbf} and all the spin parameters and angles (each one consisting of three cells). This yields a continuous version of $\chi^2_k(\mathbf{v})$ around $\mathbf{v}_{\mathrm{gbf}}$, $\chi^2(\mathbf{v})$. Thus, during the error estimation we use the $\chi^2_k(\mathbf{v})$ space around the best-fitting grid model parameters covering $5 \times 3 \times 3 \times 5 = 225$ grid-cells, leaving the power-law model parameters $\{A, s\}$ to vary freely. Since $\mathbf{v}_{\mathrm{gbf}}$ has been derived from the grid-cells (i.e. fixed values) during the error estimation process lower values of $\chi^2(\mathbf{v})$ are emerging for intermediate grid-cell values within the selected best-fitting parameter region. This are the final best-fitting parameter values that we keep from our fitting process, $\mathbf{v}_{\mathrm{bf}} = \{M_{\mathrm{bf}}, \alpha_{\mathrm{bf}}, \theta_{\mathrm{bf}}, h_{\mathrm{bf}}, A_{\mathrm{bf}}, s_{\mathrm{bf}}\}$.

Despite the fact that we can not visualize the interpolated $\chi^2(\mathbf{v})$ space due to its high dimensionality (6-dimensions) in Appendix A2 (Fig. A4, A5, A6) we show the interpolated versions of the reflected components, $\tau_{\nu}(M, \alpha, \theta, h)$, which are the actual discrete components that we interpolate in equation 13 which appear via $TL_{f_{\mathrm{bin},i}}(\mathbf{v})$ (equation 12).

Some important points of the overall procedure:

- The best-fitting values derived from the grid parameter space, $\mathbf{v}_{\mathrm{gbf}}$, are, in fact, very close to the best-fitting values derived from the interpolated parameter space, $\mathbf{v}_{\mathrm{bf}}$. All the $\mathbf{v}_{\mathrm{gbf}}$ lie within the 86.6 per cent confidence intervals (1.5 standard deviations) of the best-fitting values of $\mathbf{v}_{\mathrm{bf}}$. Note that the only reason that we perform the interpolation in the first place is for the derivation of the 68.3 per cent confidence bands and the $\mathbf{v}_{\mathrm{bf}}$ is a natural product of this process.
- We leave the power-law parameters free since their values fix the normalisation of the overall model. Note that for a given set of physical lamp-post model parameter the negative reflected component, $\tau_{\nu}(M, \alpha, \theta, h)$ is absolutely fixed. Thus both the normalisation and the index, $\{A, s\}$, of the positive power-law component define the level of the final overall time-lag spectral model.
- The cubic interpolation, that we use for the derivation of the final best-fitting model parameters and their corresponding uncertainties, smooths the $\chi^2_k(\mathbf{v})$ space adequately in order the estimation of the various gradients (needed for the orientation of the minimisation algorithm) to become much easier. Linear or quadratic interpolation yields edges in the parameter space, higher order interpolations (i.e. greater than three) create artefacts in the parameter space. Note that spline interpolation yields equivalent results as the cubic interpolation.
- In principle, the BH mass can be left as a free fitting parameter, through equation 1, together with the power-law parameters A and s. However, such an addition slows significantly the minimization process since one has to minimise equation 13 simultaneously with another equation describing the corresponding scaling in the abscissae (i.e. frequency domain). The second equation would consist of the squared differences in the abscissae between the model and the data. For the needs of this paper and the quality of our time-lag spectra the grid approach for the BH masses is very robust.

6 RESULTS

The observed time-lag spectra for all the 12 AGN together the best-fitting overall time-lag spectral models for all the sources are shown in Fig. 8. The filled circles correspond to the time-lag estimates with a coherence greater than 0.15 (Sect. 4.2) and the open circles to those time-lag estimates with coherence smaller than 0.15 (i.e. those excluded from the fitting procedure). All the time-lag spectra agree very well, within the estimated errors, with those reported by De Marco et al. (2013) with the only exception being that of NGC 7469. This difference could be caused by the slightly different selection of beginning and end times or/and by the different version of the Current Calibration Files (CCFs) which are updated on a regular basis. The best-fitting overall time-lag spectral models are shown with the black line. The panels also include the constituents components of the best-fitting time-lag spectral model; the power-law and the GR reflected component with the grey- dashed and the grey-dotted line, respectively. The best-fitting parameters together with the 68.3 per cent confidence intervals are given in Table 2.

6.1 The best-fitting BH masses

In order to check the validity of our best-fitting results, in Fig. 9 we plot the derived best-fitting BH masses (Table 2, second column) versus those originating from the existing in the literature (Table 1, first column). The literature values

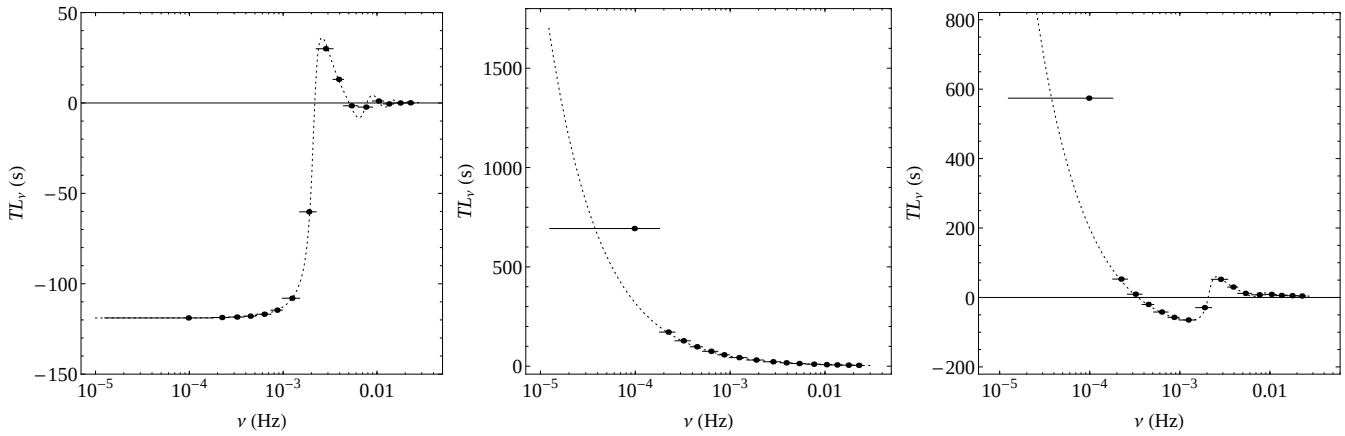

Figure 7. Discretization and averaging effects for the lamp-post case model with $\alpha = 0.676$, $\theta = 20°$, $h = 33.1$ for M=$2 \times 10^6 M_\odot$ and power-law parameters $A = 0.2$ and $s = 0.8$. The continuous models are shown with the dotted lines and the corresponding discrete estimates (averaged over the frequency ranges indicated by the horizontal lines) with the filled circles. Left-hand panel: The GR reflected component. Middle panel. The power-law component. Left-hand panel: The overall time-lag model.

Table 2. The best-fitting time-lag spectra models consisting of the GR reflected component and the power-law (PL). The first column, (1), is the name of the AGN source, the next four columns, (2,3,4 and 5), are the model parameters of the GR lamp-post component (reflected component). The next two columns, (6 and 7), are the model parameters of the power-law. The last column, (8), is the χ^2 indicator coming from the interpolated region around $\chi^2_k(\mathbf{v})$. The quoted errors correspond to the 68.3 per cent confidence intervals around the best-fitting model parameters with '—' indicating the cases where the uncertainty could not be estimated due to the finite extension of the interpolated grid.

(1) AGN name	(2) BH mass M ($\times 10^6$ $M_\odot$)	(3) BH spin α	(4) Viewing angle $\theta°$	(5) Height h (r_g)	(6) PL normalisation A (s)	(7) PL index s	(8) $\chi^2(\mathbf{v})$/d.o.f.
NGC 4395	$0.41^{+0.19}_{-0.29}$	$0.12^{+0.42}_{---}$	22^{+18}_{---}	$51.5^{+21.2}_{-36.8}$	$\left(1.3^{+0.8}_{-0.6}\right) \times 10^{-7}$	$2.4^{+0.4}_{-1.3}$	6.24
NGC 4051	$1.9^{+1.3}_{-1.1}$	$0.23^{+0.31}_{---}$	31^{+6}_{-8}	$6.3^{+2.2}_{-3.8}$	$2.3^{+0.3}_{-0.2}$	$0.44^{+0.15}_{-0.08}$	1.89
Mrk 766	$1.6^{+1.4}_{-1.2}$	$0.89^{+---}_{-0.33}$	38^{+7}_{-9}	$3.4^{+2.8}_{-1.8}$	$\left(1.5^{+1.1}_{-0.8}\right) \times 10^{-7}$	$2.4^{+0.3}_{-1.1}$	1.78
MCG–6-30-15	$2.1^{+0.9}_{-1.6}$	$0.98^{+---}_{-0.26}$	35^{+11}_{-8}	$2.9^{+0.4}_{-0.7}$	$0.27^{+0.4}_{-0.3}$	$0.77^{+0.2}_{-0.1}$	1.59
Ark 564	$3.5^{+1.3}_{-1.8}$	$0.05^{+0.45}_{---}$	58^{+---}_{-12}	$4.6^{+0.9}_{-0.7}$	$0.14^{+0.11}_{-0.07}$	$0.82^{+0.34}_{-0.29}$	1.77
1H 0707-495	$1.8^{+1.7}_{-1.2}$	$0.32^{+0.24}_{-0.22}$	27^{+9}_{-5}	$2.4^{+0.6}_{-0.3}$	0.62 ± 0.23	$0.61^{+0.3}_{-0.1}$	2.70
IRAS 13224-3809	$9.3^{+3.4}_{-2.9}$	$0.94^{+---}_{-0.28}$	59^{+---}_{-11}	$2.9^{+0.8}_{---}$	$\left(4.8^{+0.5}_{-0.8}\right) \times 10^{-2}$	$0.92^{+0.32}_{-0.29}$	1.93
ESO 113-G010	$7.1^{+3.8}_{-4.2}$	$0.91^{+---}_{-0.22}$	51^{+8}_{-7}	$8.8^{+0.9}_{-2.3}$	$\left(6.4^{+1.4}_{-0.9}\right) \times 10^{-2}$	$1.0^{+0.4}_{-0.8}$	1.56
NGC 7469	$13.3^{+7.1}_{-4.6}$	$0.61^{+0.22}_{-0.29}$	26^{+9}_{---}	$4.1^{+0.3}_{-0.8}$	$\left(8.2^{+2.1}_{-1.5}\right) \times 10^{-7}$	$2.2^{+0.4}_{-0.9}$	1.97
Mrk 335	$19.8^{+11.8}_{-10.5}$	$0.69^{+0.28}_{-0.31}$	41^{+8}_{-9}	$3.1^{+0.5}_{-0.6}$	$1.6 \pm 0.3 \times 10^{-2}$	$1.1^{+0.2}_{-0.4}$	1.81
NGC 3516	$52.8^{+15.2}_{-14.2}$	$0.14^{+0.35}_{---}$	39^{+12}_{-9}	$2.9^{+1.3}_{---}$	$\left(8.3^{+2.4}_{-1.9}\right) \times 10^{-10}$	2.6 ± 0.5	1.38
NGC 5548	$48.8^{+13.2}_{-12.6}$	$0.88^{+---}_{-0.42}$	47^{+13}_{-11}	$4.5^{+0.9}_{-1.1}$	$\left(3.2\times^{+1.9}_{-1.8}\right) \times 10^{-5}$	$1.7^{+0.5}_{-0.3}$	1.34

estimated using the reverberation technique are shown with the filled squares and for all the other cases with open circles.

In order to quantify the obvious correlation between the two quantities we use two simple methods. Initially we compute the Kendalls τ rank correlation coefficient (Press et al. 1992), using only the actual data values plotted in Fig. 9 i.e. ignoring their uncertainties. This gives a value of τ equal to 0.818 which corresponds to a very low probability for the null hypothesis, H_0, i.e. the two quantities are not associated, of 2.13×10^{-4}, indicating that there is a strong correlation between the corresponding BH mass estimates. Then, we fit to the data a simple linear model of the form $y = \kappa x + \lambda$, considering the uncertainties in both coordinates (Press et al. 1992). For each point a mean error is estimated for its abscissa and ordinate by averaging the corresponding upper and lower error estimate in each direction respectively. The best-fitting model (Fig. 9, black solid line) has a slope of $\kappa = 1.21^{+0.19}_{-0.18}$ and an intercept of $\lambda = -0.05^{+0.25}_{-0.36}$ and is derived from a χ^2 merit function of 2.98 for 10 d.o.f. yielding a very low probability for H_0 (i.e. obtaining by chance a value of χ^2 smaller or equal to 2.98 from an uncorrelated data of the same length) of 0.018. In the same plot we show the with the grey-dashed line the direct proportionality between the two quantities, i.e. $y = x$. As we can see the overall agreement is very good and within the quoted best-fitting parameter uncertainties the two lines are consistent with each other.

This result validates that the derived BH mass esti-

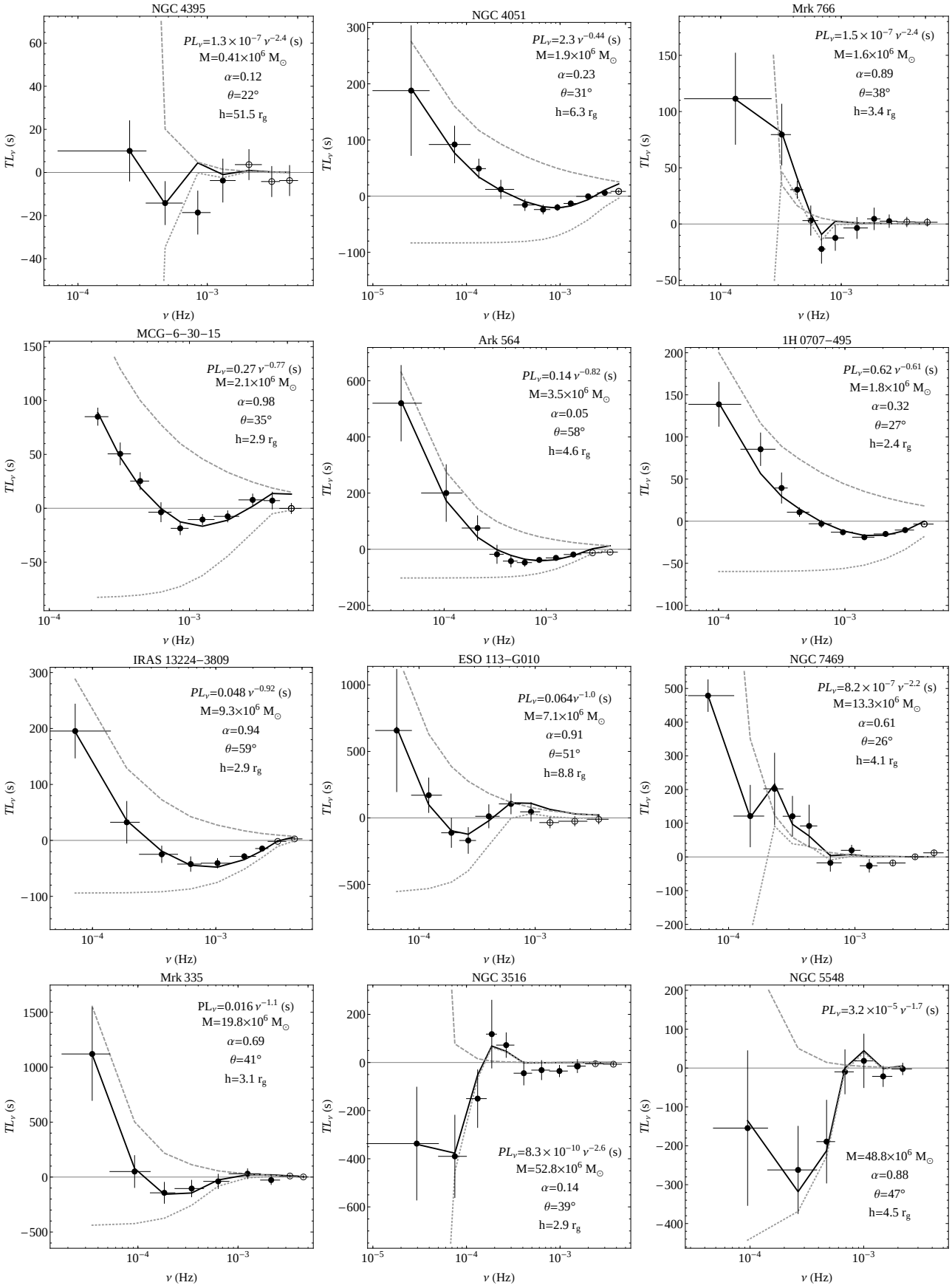

Figure 8. The best-fitting time-lag spectral models (black line) and the time-lag estimates with coherence greater than 0.15 (filled circles), –open circles correspond to lower coherence values– The two components of the best-fitting time-lag model are the GR reflected component (grey-dotted line) and the power-law (grey-dashed line).

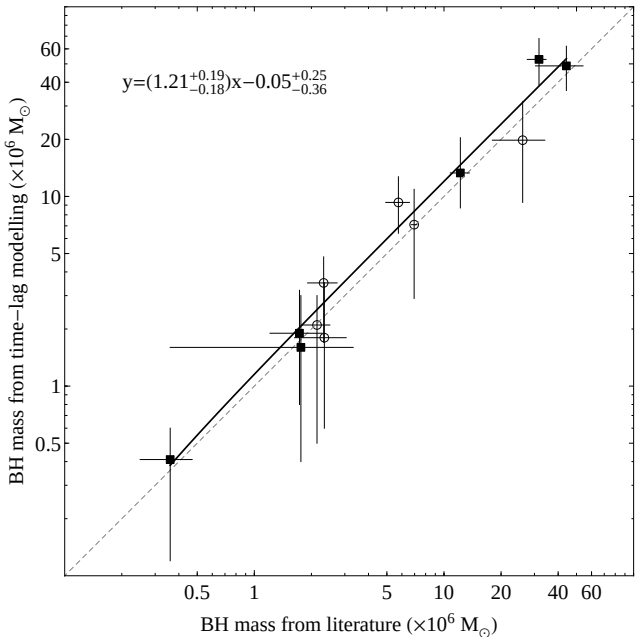

Figure 9. Best-fitting BH masses versus literature values. The filled squares correspond to the literature values estimated vie the reverberation technique (given with an (r) in the first column of Table 1) and the open circles to all the other BH mass estimates. The black solid line corresponds to the best-fitting linear model and the dashed line depicts the direct proportionality between the two quantities, $y = x$.

mates are entirely consistent with the estimates derived from other independent methods, hence supporting the validity of our modelling process and thus giving confidence in our estimation of other best-fitting lamp-post model parameters, i.e. spin, inclination and height.

6.2 The lamp-post plane and parameter correlations

In this section, we examine if there are any significant correlations between the best-fitting model parameter values. Such correlations could be of physical origin, but on the other hand, spurious dependencies could also be introduced in the presence of model degeneracies.

6.2.1 The lamp-post plane

Initially, we study the lamp-post parameter space by defining the lamp-post plane (LPP) consisting of the physical quantities of, M, α and h (θ is excluded since it is an observational property). This approach enable us to unveil potential dependencies among the various model parameters that could lead to model degeneracies. In the top panel of Fig. 10 we show the lamp-post parameter space consisting of the 12 AGN as given in Table 2. The arrows indicate the measurement error estimates that exceed the interpolated grid limits (values with '—' in Table 2).

Assuming that the LPP can be described from the equation:

$$k_M \log_{10}\left[\frac{M}{10^6 \mathrm{M}_\odot}\right] + k_\alpha \alpha + k_h \log_{10}\left[\frac{h}{r_\mathrm{g}}\right] + k_0 = 0 \qquad (14)$$

the distance of a point $\{M_i, \alpha_i, h_i\}$ from this plane is

$$\mathscr{D}_i = \frac{\left| k_M \log_{10}\left[\frac{M_i}{10^6 \mathrm{M}_\odot}\right] + c\alpha_i + k_h \log_{10}\left[\frac{h_i}{r_\mathrm{g}}\right] + k_0 \right|}{\sqrt{k_M^2 + k_\alpha^2 + k_h^2}} \qquad (15)$$

In order to derive the LPP best-fitting parameters $\{k_M, k_\alpha, k_h\}$ one can consider the total distance of all the points from the LPP and minimize it. Since the measurements are characterised by large errors in all the three directions we perform a Monte Carlo (MC) simulation. Generalising the approach employed in Sect. 6.1, we estimate for each point a mean error along each direction by averaging the corresponding upper and lower error estimates. Thus. for each point we form a three-dimension multivariate normal distribution whose probability density function is characterised by a diagonal covariance matrix, $\mathbf{\Sigma}$. This enable us to draw for each point an ensemble of 10000 random number that form around it a three dimensional ellipsoid whose axes are in the directions of the eigenvectors of $\mathbf{\Sigma}$ and the length of the i$^{\mathrm{th}}$ longest axis is proportional to $\sqrt{\lambda_i}$ where λ_i is the eigenvalue associated with the i textsuperscriptth eigenvector of $\mathbf{\Sigma}$. Finally, we find the best-fitting parameters $\{k_M, k_\alpha, k_h\}$ that minimize the total distance for each set of points and we end up with 10000 best-fitting parameters whose distribution dictates the most possible value and the corresponding uncertainties.

The best-fitting LPP by considering all the sources (Fig. 10, bottom left-hand panel) is given by the following relation

$$0.095^{+0.124}_{-0.123} \log_{10}\left[\frac{M}{10^6 \mathrm{M}_\odot}\right] - 0.018^{+0.091}_{-0.110}\alpha + 0.746^{+0.103}_{-0.084} \log_{10}\left[\frac{h}{r_\mathrm{g}}\right] - 0.526^{+0.116}_{-0.136} = 0 \qquad (16)$$

By ignoring the first AGN in the sample, NGC 4395, whose best-fitting estimates come from a very poor fit, the best-fitting LPP (Fig. 10, bottom right-hand panel) is given by:

$$-0.001^{+0.088}_{-0.082} \log_{10}\left[\frac{M}{10^6 \mathrm{M}_\odot}\right] - 0.020^{+0.086}_{-0.095}\alpha + 0.756^{+0.090}_{-0.082} \log_{10}\left[\frac{h}{r_\mathrm{g}}\right] - 0.411^{+0.096}_{-0.090} = 0 \qquad (17)$$

Both equations are consistent with each other and the best-fitting LPP parameters k_M and k_α are consistent with 0 dictating that there is no statistical coupling among the various model parameters, and thus disfavouring the existence of parameter degeneracies in our model. Both equations are consistent with an LPP plane perpendicular to the height axis (i.e. parallel to the M, α plane) intersecting with it at around h=$4.28^{+0.51}_{-0.47} r_\mathrm{g}$ (an average from the two planes).

6.2.2 Parameter correlations

In order to investigate even more the existence of potential correlations and actually visualize their nature, in the panels of Fig. 11 we plot the three lamp-post parameters, α,

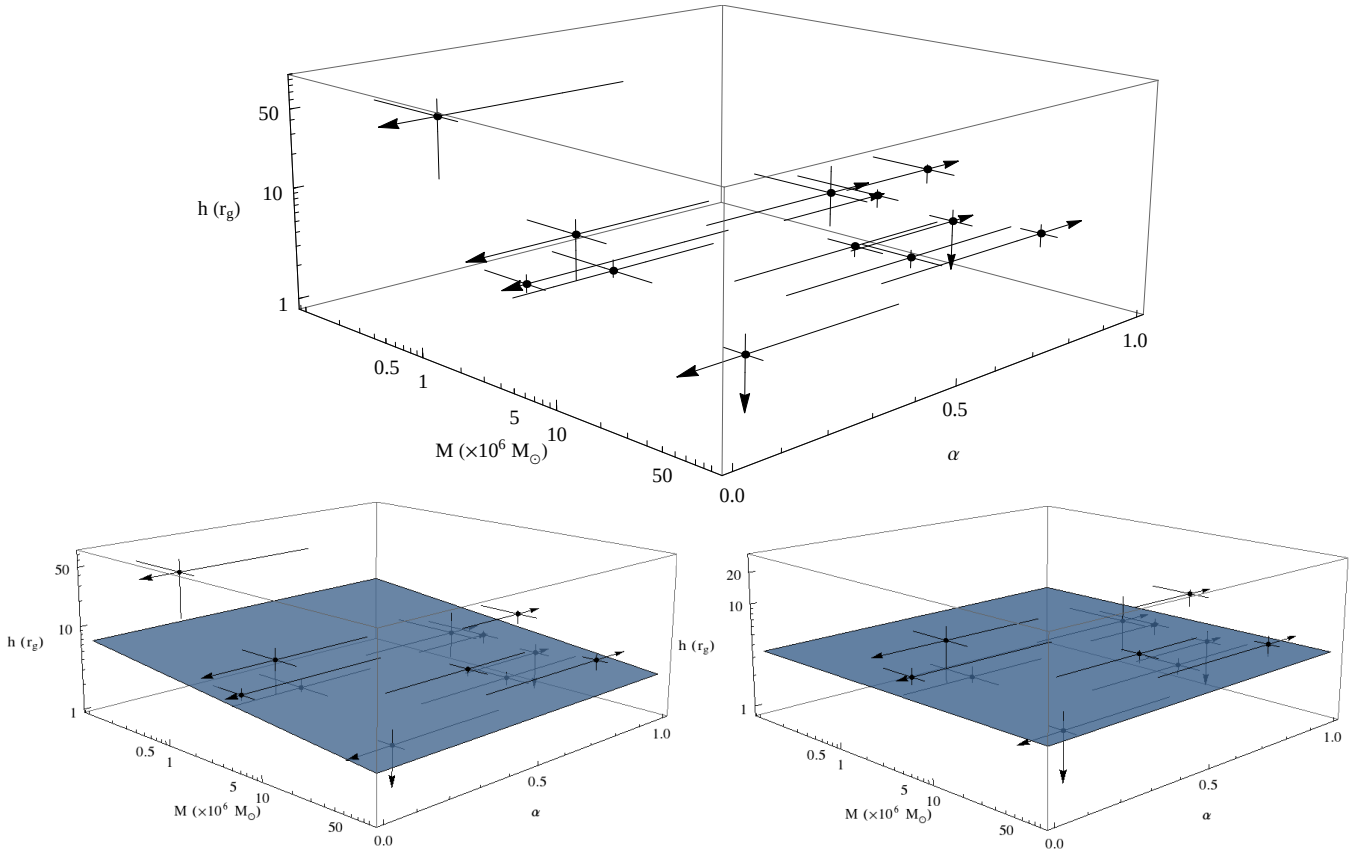

Figure 10. The lamp-post parameter space. Top panel: The values for the 12 AGN points are the best-fitting values given in Table 2. Bottom left-hand panel: The best-fitting LPP including all the AGN, given by equation 16. Bottom right-hand panel: The best-fitting LPP excluding NGC 4395, given by equation 17.

θ and h versus M. As before, the arrows indicate the measurement error estimates that exceed the interpolated grid limits (values with '—' in Table 2).

In agreement with the results of the analysis above, there is absolutely no evidence of a correlation for any of the lamp-post parameters with the BH mass. Within each panel of Fig. 11 we also quote the values of the Kendalls τ rank correlation coefficient and the corresponding probability, p, for H_0 (i.e. the two quantities are not associated). The latter values are quite large indicating that there is no ground to reject the H_0 for any of the three cases.

6.3 Best-fitting parameters

In this section we analyse each lamp-post best-fitting parameter, coming from all the sources, individually.

• Spin parameters: The effects of the spin parameter on the corresponding time-lag spectra are rather small (see Fig. A1 in Appendix A1.1) and given the quality of our X-ray data sets it is difficult to statistically distinguish between different spin-parameters, for each source individually. This is the reason for the rather large uncertainties on the model best-fitting spin parameters.

Nevertheless, the left panel in Fig. 11 suggests that there may exist two groups of objects within our sample: those with high (i.e. $\alpha \sim 1$) and those with low (i.e. $\alpha \sim 0$) BH spin parameters. To investigate a possible clustering scenario for the spin parameters, we apply an unsupervised partitioning algorithm to the derived spin parameters, using the Canberra distance (Everitt et al. 2011). Indeed, we do find that the spin parameters form two clusters of points; those defined above and below the mean value of the ensemble which is 0.62 ± 0.09, indicated by the grey-dashed line. This is indicative of two populations of objects, as we mentioned above: objects with a low and high spin. The low-spin population is characterised by a mean value of $0.35^{+0.16}_{--}$ and the high-spin population is characterised by a mean value of $0.84^{+-}_{-0.11}$.

In order to derive the probability of how significantly different these mean values are from that of the ensemble mean we perform a simple Student's t-test. For the low-spin population, the value of t-statistic is -4.55 for 5 d.o.f., yielding a small probability value for the null hypothesis, H_0, i.e. the population mean is 0.62, of 6.1×10^{-3}. Similarly, for the high-spin population the probability of H_0 is low, 1.4×10^{-3}, corresponding to a t-statistic value of 6.37 for 5 d.o.f.

We therefore find significant evidence for the presence of two groups of objects: those with high BH spin parameters (larger than 0.75) and those with a low BH spin parameters (smaller than 0.5). We note that this result should be treated with some caution, as the initial selection of points was done by our clustering algorithm, whose results are hard to judge due to the small number of objects in the original sample.

Nevertheless, what we can state with high confidence is that the α best-fitting values for the high- and low-

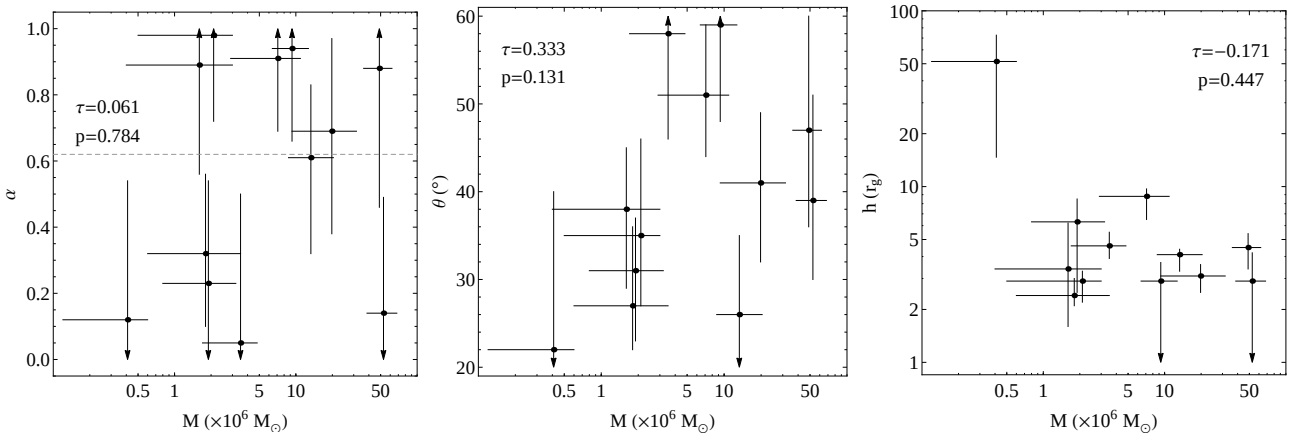

Figure 11. Correlation plots of the various best-fitting lamp-post parameters versus the best-fitting BH mass, showing also the Kendalls τ rank correlation coefficients and the corresponding probability, p, for H_0. Left-hand panel: The BH spin parameters. The grey-dashed line corresponds to the mean value of the ensemble of points, 0.62 ± 0.09. Middle panel: The viewing angles. Right-hand panel: The heights of the X-ray sources.

spin populations differ significantly from 0 and 1, respectively. Namely, for five sources: Mrk 766, MCG–6-30-15, IRAS 13224-3809, ESO 113-G010 and NGC 5548, the derived spin parameter values differ significantly from 0, with H_0 (i.e. the quantity is consistent with zero) probabilities of 0.0034, 8.19×10^{-5}, 3.94×10^{-4}, 1.76×10^{-5} and 0.018, respectively. On the other hand, the spin parameters for five AGN: NGC 4395, NGC 4051, Ark 564, 1H 0707-495 and NGC 3516, differ significantly from 1, having H_0 (i.e. the quantity is consistent with one) probabilities of 0.018, 0.006, 0.017, 0.002 and 0.007, respectively. Thus, not all AGN have a maximally/minimally spinning BHs, and more importantly the actual value of the BH does not correlate with the BH mass i.e. Schwarzschild and Kerr BHs can exist in AGN with the same mass.

• Angles: The viewing angles are distributed uniformly between 20 to 60° with a mean value of $39.5^{+4.9}_{-4.3}{}^{\circ}$. Within the unification models for AGN, this result would imply an average opening angle (i.e. twice the viewing angle) for the putative molecular torus of around $80^{+9.8}_{-8.6}{}^{\circ}$. This is in agreement with recent results which find a Type II to Type I AGN ratio of the order of 1.75 (Rush et al. 1993; Burlon et al. 2011; Toba et al. 2013). This ratio implies a TypeI/(TypeI+TypeII) ratio of around 0.35, and hence an opening angle of the torus of around 100°. We consider this agreement as another indication that our approach yields reasonable values for the best-fit model parameters. However note that, as in the case of the spin parameter, the effects on the viewing angles to the corresponding time-lag spectra are also rather small (see Fig. A2 in Appendix A1.2).

• Heights: The 'lamp' height is the best constrained fitting parameter (i.e. has the smallest error). As we can see from Fig. A3 in Appendix A1.3 this is due to the fact the X-ray source height affects significantly the form of the corresponding time-lag spectra, since the onset of the initial negative plateau as well as the strength and the position of peaks is greatly modified by different heights of the X-ray source. The particularly low best-fitting values for the height parameter indicate that, within the lamp-post geometry model, the X-ray source is situated very close to the BH. The mean average value of the height is $3.72^{+0.56}_{-0.52}$ $r_{\rm g}$ including the first estimate of NGC 4395 (first point) coming from a very poor fit. Thus, the small heights indicate that for all AGN (within the lamp-post model scenario) the X-ray source has a rather small size and it is situated very close the BH, hence should also have a rather small size. This, is a solid result which does not suffer from model degeneracies as we showed in the previous section (Sect. 6.2.1).

6.4 Mass scaling relation

De Marco et al. (2013) have shown that for each source, from an ensemble of 15 AGN, the most negative time-lag value and the corresponding frequency scales linearly, in logarithmic space, with its BH mass. As we find from our physical modelling, the principal parameters affecting the form of the negative component of the time-lag spectra is the BH mass as well as the height of the X-ray source. As we show in the previous section (Sect. 6.3), in almost all the AGN the X-ray source lies above the accretion disc at the same small height, around 3–4 $r_{\rm g}$ above the BH. Thus, the De Marco et al. (2013) relation holds because the source height appears to be comparable in all AGN, but also because the BH mass range is sufficiently small that, within the frequency range sampled by *XMM-Newton*, we measure the same part of the time-lag spectrum in almost all AGN.

To clarify this issue, in Fig. 12 we plot the negative model components of the time-lag spectra (discretized and binned in order to mimic the observations –see Sect. 5 and Fig. 7–) for objects with BH masses in the range between $10^4 - 10^8$ $M_\odot$. The arrows, in the same figure, indicate the most-negative time-lag measurements in each case. Clearly, within the observed frequency range, the larger the BH mass, the larger the most-negative time delay and the lower the corresponding frequency. The frequency range over which the time-lags spectra have been estimated corresponds to the frequency range (i.e. between 10^{-5} Hz and few times 10^{-3} Hz) that is currently 'available' with the present day *XMM-Newton* observations. As we can see from Fig. 12, within this frequency range, the amplitudes of the time-lag

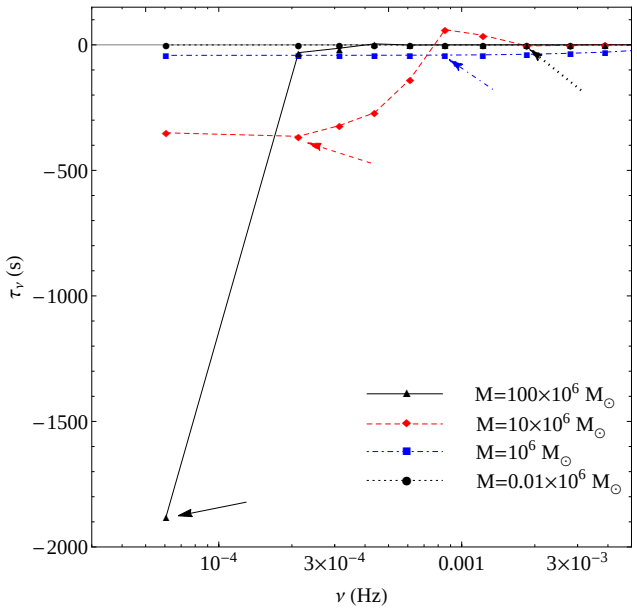

Figure 12. The mass scaling relation. The discretized negative time-lag spectral component for the lamp-post models with $\alpha = 1$, $\theta = 40°$and $h = 3.6\ r_{\rm g}$ and BH masses: $M = (0.01, 1, 10, 100) \times 10^6\ {\rm M}_\odot$. The arrows indicate the most negative time-lag point for each BH mass. –A colour version of this figure is available in the online version of the journal–

spectra indeed become smaller with increasing frequency. However, if we had longer observations (e.g. going down to 10^{-8} Hz) then the time-lag values for the highest BH mass would be larger at frequencies below those presently observable. Alternatively, if the observation length was shorter so than the lowest observed frequency for the same BH mass was *higher* than $\sim 2 \times 10^{-4}$ Hz, then the 'most-negative' time-lag estimate would certainly be less than the maximum negative time-lag for this object. We therefore caution the readers that *the most negative time-lag value and the corresponding frequency versus BH mass scaling relations* hold for objects with a BH mass not larger than $10^8\ {\rm M}_\odot$, as long as the X-ray source is situated on the same height for all objects, and the time-lags have been estimated in a *same* frequency range which is the same as the one used by De Marco et al. (2013).

7 SUMMARY AND DISCUSSION

We have modelled the time-lag spectra of 12 AGN, using with the highest-quality *XMM-Newton* observations, in terms of signal-to-noise ratio and observational length. We have employed physically realistic GRIRFs for the case of the lamp-post geometrical model in which the X-ray source lies above the BH. This is the first time that such a fully GR approach is employed to model in a statistically robust way the time-lags spectra of a large number of local AGN. Our results imply that such a model can adequately describe the observed X-ray time delays and thus it is a realistic representation of the innermost regions of most AGN.

We find that the observed time-lag spectra of all objects are fully consistent with the hypothesis of X-ray reverberation from the innermost part of the accretion disc. The main results from our analysis are summarised below.

- The best-fitting BH-masses are in very good accordance with those derived from other, independent, methods, e.g. optical reverberation mapping.
- The best-fitting viewing angles imply an opening angle of around 80° for the putative molecular torus, which is fully consistent with current estimates for the ratio of Type II over Type I Seyfert galaxies in the local Universe.
- There is no correlation between the BH mass and any of the lamp-post model parameters, i.e. spin, viewing angle and height (Fig. 11).
- There is a tentative evidence for bimodality in the distribution of the best-fitting spin parameters above and below $\alpha = 0.62$: one group with a low BH-spin (with a mean of 0.35) and another group with a high BH spin (with a mean of 0.84), respectively. In any case, our results indicate, with a high significance, that the BH spin for member of the former group is not consistent with 1, while the BH spin for the objects in the latter group is not consistent with 0. But we do not find any correlation between BH mass and BH spin: our results suggest the existence of both Schwarzschild and Kerr BHs, at any given BH mass.
- The average X-ray source height is $3.7 r_{\rm g}$, with little dispersion. As these heights are an approximation to the X-ray source size, these results imply a very small source size.

Our modelling is limited by a few assumptions, which can potentially affect the validity of our results. To start with, as we have mentioned in Sect.3.2, strictly speaking, our GRIRFs do not correspond to the actual response of the soft band but rather to the response of the neutral fluorescent Fe Kα line, at 6.4 keV (in the rest frame of the accretion disc). However, if both the Fe Kα line and the soft band photons are generated in the same part of the disc, there should not be dramatic differences between the two GRIRFs. Perhaps, more important may be our assumption of the contribution of the reflection spectrum in the soft band to 30 per cent of the total observed flux for all objects, and our assumption of neglecting the presence of a reflection component in the 2–4 keV energy band, which we considered as a proxy for the direct continuum emission. This issue has been discussed by Wilkins & Fabian (2013), who show that the presence of a reflection continuum in the continuum hard band does affect the strength of the reflection component in the resulting time-lags spectra. Full investigation of this issue would have been computationally prohibitive in our case, where we try to model the time-lags spectra of a large number of AGN. Nevertheless, we believe that the good agreement between the BH mass estimates, from the present work, and the estimates resulting from other independent methods, as well as the reasonable estimates we get for the viewing angles for all the objects in the sample, imply that our results should be a valid representation of the true values of the other model parameters (i.e. BH spin and X-ray source height and size) as well. This could possibly also indicate that, based on the current data quality, we are not able to discern significant differences in the fitting parameters between the actual response of the soft band and that of the neutral Fe Kα line.

We note in passing that, given the good agreement between the BH estimates presented in this work, and others

from the literature, the time-lag spectrum modelling with physically motivated models, is yet another way of measuring the BH mass in these systems. The uncertainty of our BH mass estimates is rather large, but this is not due to the method itself, but rather to the quality of the available time-lags spectra, even though we have used the longest X-ray data sets currently available obtained by *XMM-Newton*. In the case of objects with a BH mass larger than few times 10^7 $M_\odot$, the main limitation arises from the duration of the available X-ray light curves. For these objects, all the largest amplitudes time-lag spectral features (e.g. the the most negative time-lag estimate) are shifted towards frequencies which are lower than the lowest accessible frequency from our current light curves, which consist, in the best cases, of around 120 ks, or few times 10^{-5} Hz in the frequency domain. As a result, the only time-lag spectral features available to fit are of small amplitude, resulting in larger BH mass fitting uncertainties (i.e. the χ^2 regions around the best fitting-values are characterised by a smaller curvature and thus larger errors).

From the other hand, for objects with smaller BH mass, below 10^6 $M_\odot$, the largest time-lag amplitude variations are shifted towards the high Fourier frequencies above few times 10^{-3} Hz. In these frequencies, due to the Poisson noise, the very low coherence of our light curves prohibits any meaningful physical modeling. Thus, in these cases we need to sample thoroughly the small time-scales in order to determine accurately the various lamp-post model parameters; something which is beyond the sensitivity limit of current X-ray observatories.

Both of these observational problems will be solved by future X-ray observatories. Athena, due for launch in 2028, will be placed at the L2 point and so will allow continuous uninterrupted observations for as long as it is needed, in order to sample completely the low frequency part of the time-lag spectra of the high BH mass AGN. Athena will also have almost an order of magnitude greater sensitivity than *XMM-Newton*, allowing detailed measurements of the time-lags in the high frequency domain. Moreover, if approved, LOFT, although not allowing long continuous observations, will improve sensitivity at high frequencies due to its superior effective area.

A major result from our analysis is that the height of the X-ray source must be very close to the BH, around 3.7 $r_{\rm g}$, in all AGN. In the lamp-post geometry layout this X-ray source should somehow correspond to the centroid of a hemispherical X-ray corona lying above the accretion disc (a similar X-ray source exists below the disc) where the bulk of the hard X-rays are produced. The derived compactness of the X-ray region and its proximity to the central BH is in accordance with recent X-ray microlensing studies (Chartas et al. 2009, 2012), who also find values for the X-ray source size as small as 6–10 $r_{\rm g}$. The lack of correlation between the height and either the mass and/or the BH spin spin indicates that the dimensions of the X-ray region must by tuned by some other physical parameters, perhaps the (currently unknown) physical mechanism which generates this X-ray emission, which should be the same in all objects. Note that if there was any height-luminosity dependence, it would have been wiped out since we are using luminosity-averaged time-lag spectra. In a future work we will address this issue by modelling the time-lag spectra during high and low source states.

Another major result from our work is that the BH spin parameter, α, does *not* appear to be the same in all objects. We find that five sources in our sample, namely Mrk 766, MCG–6-30-15, IRAS 13224-3809, ESO 113-G010 and NGC 5548, possibly host a rotating BH, since the best-fitting α for these objects differs significantly from zero. On the other hand, the best-fitting spin parameters differ significantly from unity in the case of NGC 4051, Ark 564, 1H 0707-495 and NGC 3516 suggesting that they may host a non-rotating BH. Reynolds (2013) considered a sample of 20 AGN and, by compiling X-ray spectral fitting from the literature, found high spin parameter values ($\alpha > 0.8$) for $M = \left(2 \times 10^6 - 3 \times 10^7\right)$ $M_\odot$, with a hint of lower values ($\alpha \simeq 0.5$) for $M < 2 \times 10^6$ and $M > 5 \times 10^7$ $M_\odot$, favouring a prolonged ordered (coherent) accretion scenario that spins up the BH to high values. Our results are in agreement with theirs, although we do not observe a correlation between BH spin and mass. This may be due to the rather small size of our sample. On the other hand, our results i.e. high and low spin parameters and the lack of correlation between α and M, favour a galaxy mergers scenario, in which the BH growth occurs in gas-poor galaxies, resulting to a distribution of spins that has little dependence on BH mass (Volonteri et al. 2013).

Our work shows that derivation of the geometry of the X-ray source and surrounding reprocessing material (here modelled as an accretion disc) in the vicinity of BHs is possible from studies of the Fourier-resolved time-lags, between soft and hard X-ray bands. In future papers, we will study, via GR ray tracing, X-ray photons of all energies as they are reflected and reprocessed by the accretion disc. Not only will we then be able to properly trace the behaviour of soft photons, after they are emitted from the disc, but we will also be able to determine the contribution of reflected photons to the observed 1.5–4 keV hard X-ray band. At the same time, we will model separately the high and low X-ray flux states of all AGN, in order to trace possible luminosity dependencies with respect to the X-ray source height. With future X-ray observatories such as Athena and LOFT it will be possible to improve significantly on our present time-lag spectral estimates by extend them to a much wider mass range and decreasing their uncertainties.

ACKNOWLEDGMENTS

DE and IMM acknowledge the Science and Technology Facilities Council (STFC) for support under grant ST/G003084/1. The research leading to these results has received funding from the European Union Seventh Framework Programme (FP7/2007–2013) under grant agreement №312789. This research has made use of NASA's Astrophysics Data System Bibliographic Services.

REFERENCES

Arévalo P., Papadakis I. E., Uttley P., McHardy I. M., Brinkmann W., 2006, MNRAS, 372, 401
Beckwith K., Done C., 2004, MNRAS, 352, 353

Bendat J. S., Piersol A. G., 1986, Random Data: Analysis and Measurement Procedures. New York: John Wiley & Sons, —c1986, 2nd ed.
Bentz M. C., et al., 2009, ApJ, 705, 199
Bevington P. R., Robinson D. K., 1992, Data reduction and error analysis for the physical sciences. New York: McGraw-Hill, —c1992, 2nd ed.
Burlon D., Ajello M., Greiner J., Comastri A., Merloni A., Gehrels N., 2011, ApJ, 728, 58
Cackett E. M., Fabian A. C., Zogbhi A., Kara E., Reynolds C., Uttley P., 2013, ApJ, 764, L9
Campana S., Stella L., 1995, MNRAS, 272, 585
Cappi M., 2006, Astronomische Nachrichten, 327, 1012
Chainakun P., Young A. J., 2012, MNRAS, 420, 1145
Chartas G., Kochanek C. S., Dai X., Moore D., Mosquera A. M., Blackburne J. A., 2012, ApJ, 757, 137
Chartas G., Kochanek C. S., Dai X., Poindexter S., Garmire G., 2009, ApJ, 693, 174
Crummy J., Fabian A. C., Gallo L., Ross R. R., 2006, MNRAS, 365, 1067
De Marco B., Ponti G., Cappi M., Dadina M., Uttley P., Cackett E. M., Fabian A. C., Miniutti G., 2013, MNRAS, 431, 2441
Denney K. D., et al., 2010, ApJ, 721, 715
Done C., Davis S. W., Jin C., Blaes O., Ward M., 2012, MNRAS, 420, 1848
Dovčiak M., Karas V., Matt G., 2004, MNRAS, 355, 1005
Dovčiak M., Muleri F., Goosmann R. W., Karas V., Matt G., 2011, ApJ, 731, 75
Dumont A.-M., Abrassart A., Collin S., 2000, A&A, 357, 823
Emmanoulopoulos D., McHardy I. M., Papadakis I. E., 2011, MNRAS, 416, L94
Everitt B. S., Landau S., Leese M., Stahl D., 2011, Cluster Analysis. London: John Wiley and Sons Limited, —c2010, 5th ed. Series in Probability and Statistics
Fabian A. C., et al., 2013, MNRAS, 429, 2917
Fabian A. C., Rees M. J., Stella L., White N. E., 1989, MNRAS, 238, 729
Fabian A. C., et al., 2009, Nature, 459, 540
Gabriel C., et al., 2004, in Astronomical Society of the Pacific Conference Series, Vol. 314, Astronomical Data Analysis Software and Systems (ADASS) XIII, F. Ochsenbein, M. G. Allen, & D. Egret, ed., pp. 759–+
George I. M., Fabian A. C., 1991, MNRAS, 249, 352
Grier C. J., et al., 2012, ApJ, 744, L4
Gültekin K., et al., 2009, ApJ, 698, 198
Kotov O., Churazov E., Gilfanov M., 2001, MNRAS, 327, 799
Krommer A. D., Ueberhuber C. W., 1998, Computational Integration. Philadelphia: SIAM, —c1998, 1st ed.
Krug H. B., Rupke D. S. N., Veilleux S., 2010, ApJ, 708, 1145
Laor A., 1991, ApJ, 376, 90
Legg E., Miller L., Turner T. J., Giustini M., Reeves J. N., Kraemer S. B., 2012, ApJ, 760, 73
Malcolm M. A., Simpson R., 1975, ACM Trans. Math. Softw., 1, 129
Malkan M. A., 1983, ApJ, 268, 582
McHardy I. M., Arévalo P., Uttley P., Papadakis I. E., Summons D. P., Brinkmann W., Page M. J., 2007, MNRAS, 382, 985
McHardy I. M., Gunn K. F., Uttley P., Goad M. R., 2005, MNRAS, 359, 1469
McHardy I. M., Papadakis I. E., Uttley P., Page M. J., Mason K. O., 2004, MNRAS, 348, 783
Miller L., Turner T. J., Reeves J. N., Braito V., 2010, MNRAS, 408, 1928
Miyamoto S., Kitamoto S., 1989, Nature, 342, 773
Nowak M. A., Vaughan B. A., 1996, MNRAS, 280, 227
Nowak M. A., Vaughan B. A., Wilms J., Dove J. B., Begelman M. C., 1999, ApJ, 510, 874
Page K. L., Turner M. J. L., Done C., O'Brien P. T., Reeves J. N., Sembay S., Stuhlinger M., 2004, MNRAS, 349, 57
Papadakis I. E., Nandra K., Kazanas D., 2001, ApJ, 554, L133
Peterson B. M., et al., 2005, ApJ, 632, 799
—, 2004, ApJ, 613, 682
Pietsch W., Bischoff K., Boller T., Doebereiner S., Kollatschny W., Zimmermann H.-U., 1998, A&A, 333, 48
Press W. H., Teukolsky S. A., Vetterling W. T., Flannery B. P., 1992, Numerical recipes in FORTRAN. The art of scientific computing. Cambridge: University Press, —c1992, 2nd ed.
Priestley M. B., 1981, Spectral Analysis and Time Series: Probability and Mathematical Statistics, Vol. 1-2. London: Academic Press, —c1981
Reynolds C. S., 2013, Space Sci. Rev., 81, eprint:1302.3260
Reynolds C. S., Young A. J., Begelman M. C., Fabian A. C., 1999, ApJ, 514, 164
Risaliti G., Elvis M., Nicastro F., 2002, ApJ, 571, 234
Romano P., et al., 2004, ApJ, 602, 635
Rush B., Malkan M. A., Spinoglio L., 1993, ApJS, 89, 1
Shakura N. I., Sunyaev R. A., 1973, A&A, 24, 337
Sriram K., Agrawal V. K., Rao A. R., 2009, ApJ, 700, 1042
Strüder L., et al., 2001, A&A, 365, L18
Toba Y., et al., 2013, PASJ, 65, 113
Tombesi F., Cappi M., Reeves J. N., Palumbo G. G. C., Yaqoob T., Braito V., Dadina M., 2010, A&A, 521, A57
Vaughan B. A., Nowak M. A., 1997, ApJ, 474, L43+
Vestergaard M., Peterson B. M., 2006, ApJ, 641, 689
Volonteri M., Sikora M., Lasota J.-P., Merloni A., 2013, ApJ, 775, 94
Wang J.-M., Netzer H., 2003, A&A, 398, 927
Wilkins D. R., Fabian A. C., 2013, MNRAS, 430, 247
Zhou X.-L., Wang J.-M., 2005, ApJ, 618, L83
Zoghbi A., Fabian A. C., Uttley P., Miniutti G., Gallo L. C., Reynolds C. S., Miller J. M., Ponti G., 2010, MNRAS, 401, 2419
Zoghbi A., Uttley P., Fabian A. C., 2011, MNRAS, 412, 59

APPENDIX A: EXPLORATION OF THE MODEL PARAMETER SPACE

In this section we explore the model parameter space in order to visualize and understand the effect of the various parameters to the resulting GRIRFs and the corresponding time-lag spectra. Note that colour versions of all the figures in the Appendix are available in the online version of the journal.

A1 The lamp-post model parameters

For each case we vary a single model parameter leaving the rest fixed to some typical values: $M = 2 \times 10^6$ M$_\odot$, $\alpha = 0$, $\theta = 40^\circ$ and $h = 7\ r_{\rm g}$.

A1.1 The BH spin parameter, α

In this section we vary the spin parameter of the BH between the three values (i.e. Schwarzschild, intermediate and Kerr). Geometrically this changes the inner radius of the accretion disc $r_{\rm in}$ (see Sect.3.1). As we can see from the left-hand panel of Fig.A1 the GRIRFs (left-hand panel) differ mainly around the two peaks. The two extreme cases, i.e. Schwarzschild ($\alpha = 0$) and Kerr ($\alpha = 1$), differ significantly from each other but not so much with the intermediate case ($\alpha = 0.676$). The corresponding time-lag spectra (Fig.A1, right-hand panel) differ mainly around the level of the negative plateau between the frequencies $\left(10^{-5} - 10^{-4}\right)$ Hz, and the first most positive peak (inset). Again the differences between the three cases are more prominent for the two extreme cases.

A1.2 The viewing angle, θ

Here we vary the viewing angle between the three values (i.e. θ =20, 40 and 60°). This changes the position of the earliest iso-delay surface that intersects with the accretion disc and thus it affects the onset of the X-ray reverberation phenomenon described by the GRIRF. As we can see in the left-hand panel of Fig. A2, the greater the viewing angle the earliest the starting time of the reflection on the disc. Furthermore this changes the ratio height of the two peaks increasing the second peak with decreasing angle. The corresponding time-lag spectra differ significantly from each other, showing distinct features across the the whole frequency range (i.e. negative plateau and region around the first positive peak).

A1.3 The X-ray source height, h

In this section we vary the height of the X-ray source between three values, h =2.3, 33.1 and 80.2 $r_{\rm g}$. These geometric alterations affect the path-length followed by the hard X-ray photons on their way to the accretion disc. That means that the higher the source the longer the distance (even in the simple Newtonian case) and thus the later the onset of the X-ray reverberation phenomenon. Exactly this behaviour is depicted by the corresponding GRIRFs in the left-hand panel of Fig. A3, left-hand panel). For these cases, the time-lag spectra cover, as expected, different frequency range and they are not 'shifted versions' of each other.

A2 Interpolated time-lag spectra

In this section we plot the interpolated versions for the time-lag spectra of the reflected components $\tau_\nu(M, \alpha, \theta, h)$ that are used to create the interpolated version of $\chi^2_k(\mathbf{v})$, $\chi^2(\mathbf{v})$ (Sect. 5). In Fig. A5, A4 and A6 we plot the interpolated versions of the time-lag spectra for the spin, the angle, and the height, respectively.

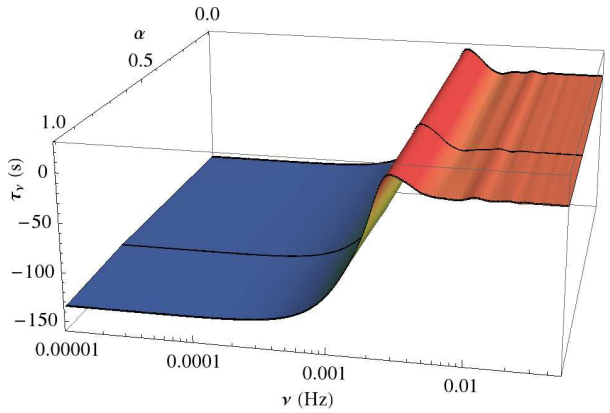

Figure A4. Spin parameter interpolation for the lamp-post model with $\theta = 40^\circ$, and $h = 7\ r_{\rm g}$, for $M = 2 \times 10^6$ M$_\odot$. The cubic interpolation of the various time-lag estimates between the spin parameters 0, 0.676 and 1 indicated by the thick lines on the surface.

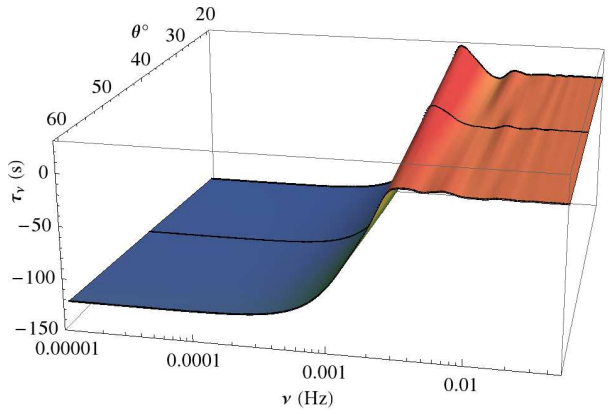

Figure A5. Viewing angle interpolation for the lamp-post model with $\alpha = 0$, and $h = 7\ r_{\rm g}$, for $M = 2 \times 10^6$ M$_\odot$. The cubic interpolation of the various time-lag estimates between the angles 20, 40 and 60° indicated by the thick lines on the surface.

This paper has been typeset from a TEX/ LATEX file prepared by the author.

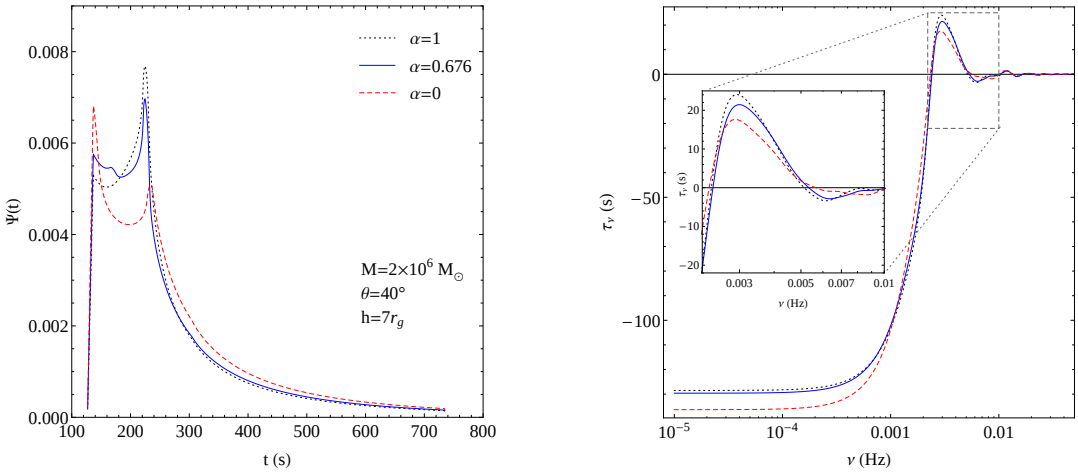

Figure A1. BH spin parameter variation for the lamp-post model with $\theta = 40°$ and $h = 7\ r_{\rm g}$, for $M = 2 \times 10^6\ {\rm M}_\odot$. Left-hand panel: The GRIRFs for three types of spin parameter, α =0, 0.676 and 1. Right-hand panel: The corresponding time-lag spectra.

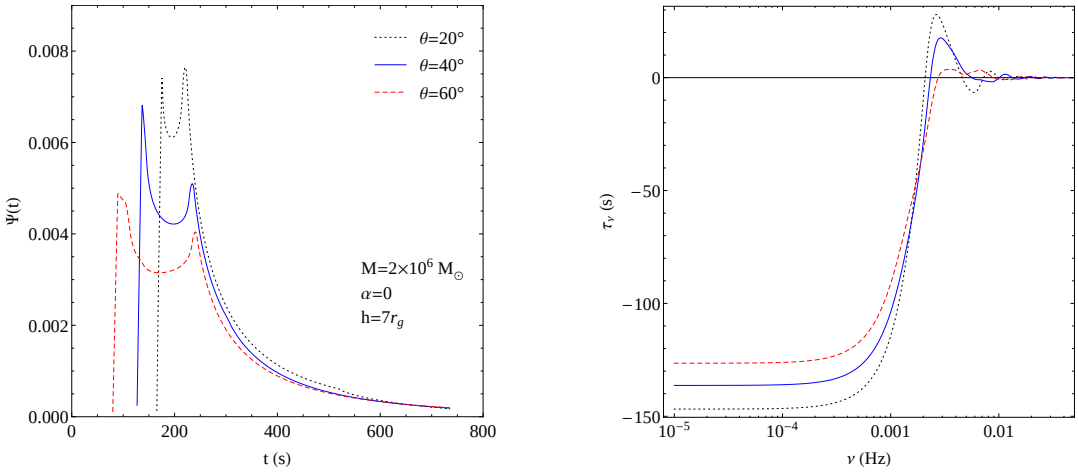

Figure A2. Viewing angle variation for the lamp-post model with $\alpha = 0$, and $h = 7\ r_{\rm g}$, for $M = 2 \times 10^6\ {\rm M}_\odot$. Left-hand panel: The GRIRFs for three viewing angles, θ =20, 40 and 60°. Right-hand panel: The corresponding time-lag spectra.

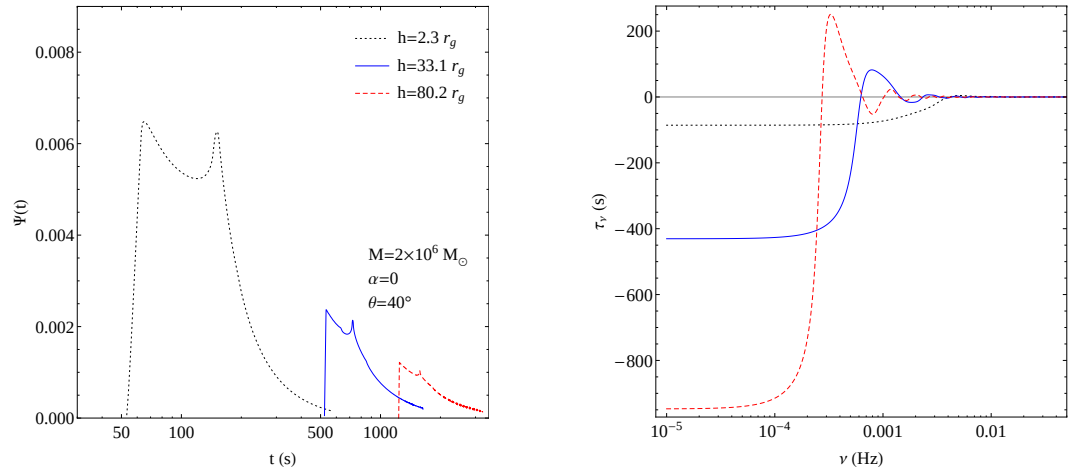

Figure A3. X-ray source's height variation for the lamp-post model with $\alpha = 0$, $\theta = 40°$, for $M = 2 \times 10^6\ {\rm M}_\odot$. Left-hand panel: The GRIRFs for three heights, h =2.3, 33.1 and 80.2 $r_{\rm g}$. Right-hand panel: The corresponding time-lag spectra.

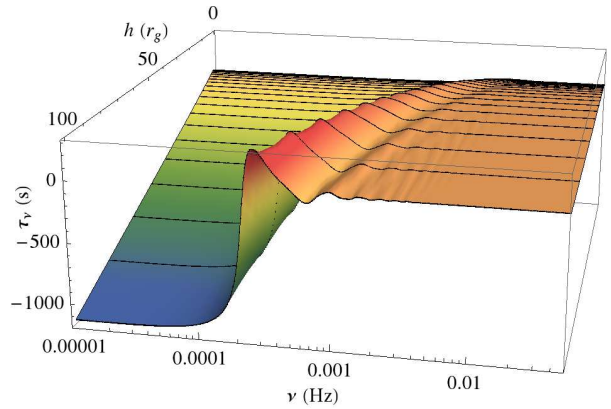

Figure A6. Height parameter interpolation for the lamp-post model with $\alpha = 0$, $\theta = 40°$, for $M = 2 \times 10^6$ $M_{\odot}$. The cubic interpolation of the various time-lag estimates between the 18 heights from 2.3 r_g to 100 r_g indicated by the thick lines on the surface.